HUMAN DEVELOPMENT

Gastruloids enable modeling of the earliest stages of human cardiac and hepatic vascularization

Oscar J. Abilez†* Huaxiao Yang†, Yuan Guan, Mengcheng Shen, Zehra Yildirim, Yan Zhuge, Ravichandra Venkateshappa, Shane R. Zhao, Angello H. Gomez, Marcel El-Mokahal, Logan Dunkenberger, Yoshikazu Ono, Masafumi Shibata, Peter N. Nwokoye, Lei Tian, Kitchener D. Wilson, Evan H. Lyall, Fangjun Jia, Hung Ta Wo, Gao Zhou, Bryan Aldana, Ioannis Karakikes, Detlef Obal, Gary Peltz, Christopher K. Zarins, Joseph C. Wu*



author affiliations: https://doi.org/10.1126/ science.adu9375

INTRODUCTION: Human pluripotent stem cells (hPSCs), including human embryonic stem cells and human induced pluripotent stem cells, can differentiate into various cell types of the body, such as cardiomyocytes, hepatocytes, and individual types of vascular cells. Furthermore, hPSCs can be used to create organoids, which are self-organizing three-dimensional (3D) structures that mimic key structural and functional characteristics of their in vivo organ counterparts. Several approaches to create organoids with a vascular system have been pursued to (i) avoid necrosis in the center of organoids where oxygen tension is low; (ii) achieve larger organoid growth for improving fidelity in modeling development, modeling diseases, and discovering new drugs; and (iii) increase the viability of implanted organoids used as regenerative therapies. However, codifferentiating the key cell types of an organoid along with a de novo vasculature comprising robust branching, hierarchical organization, and lumina formation has not been fully achieved.

RATIONALE: Although model organisms have provided insight into the earliest stages of organ vascularization, we know very little about this process in humans because of ethical restrictions and the technical difficulty of obtaining human embryos at early developmental stages. However, hPSCs have been shown to model key aspects of development, including primitive streak formation, gastrulation, germ layer formation, and individual organ-specific cell type creation. Moreover, geometric micropatterning of hPSCs has enabled reproducible and scalable modeling of these developmental processes. With this basis, we developed an in vitro model to mimic the earliest developmental stages of cardiac and hepatic organoid vascularization, which corresponds to the first 3 weeks of in vivo human development and Carnegie Stages 9 and 10.

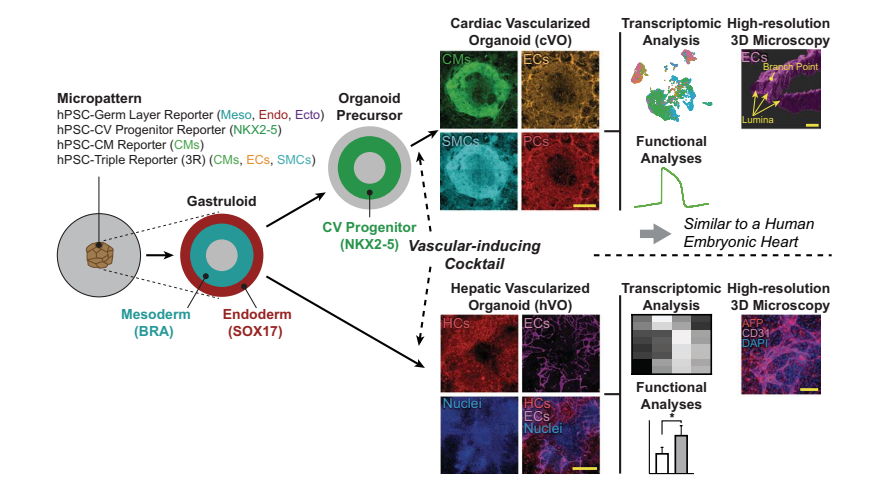
RESULTS: Using four hPSC fluorescent reporter systems and spatially micropatterned hPSCs, we produced cardiac vascularized organoids (cVOs) in a scalable and reproducible fashion. Notably, we used the four reporter systems to characterize gastruloid, progenitor, and cardiovascular cell type formation in situ in developing cVOs. We identified a growth factor and small molecule cocktail that when added to micropatterned hPSCs generated a spatially organized, branched, and lumenized vascular network within a multilineage cVO comprising endocardial, myocardial, epicardial, and neuronal cell types. Single-cell transcriptomics, high-resolution 3D microscopy, and multiple functional analyses showed that cVOs were structurally and functionally similar to that of a 6.5-postconception week human embryonic heart at Carnegie Stages 19 and 20; however, our comparison also revealed differences that warrant future investigation. Additionally, we found that NOTCH and bone morphogenetic protein (BMP) signaling were required for vascularization in cVOs, with BMP inhibition having a more negative effect on vascular formation than NOTCH. To demonstrate the broader utility of our vascularization strategy, we used the same vascular-inducing cocktail to produce hepatic vascularized organoids (hVOs), which also comprised a spatially organized, branched, and lumenized vascular network integrated with multilineage hepatic cell types.

CONCLUSION: Our in vitro model represents a technical advance for addressing questions regarding de novo organ vascularization. Furthermore, our results suggest that a conserved developmental program is involved in creating the vasculature within different organ systems.

*Corresponding author. Email: ojabilez@stanford.edu (O.J.A.); joewu@stanford.edu (J.C.W.) †These authors contributed equally to this work. Cite this article as O. J. Abilez et al., Science 388, eadu9375 (2025). DOI: 10.1126/science.adu9375

Micropatterning of four hPSC reporter lines enabled gastruloid, cardiovascular, progenitor, and cVO formation. The

identification of a vascular-inducing cocktail of growth factors enabled generation of a spatially organized, branched, and lumenized vascular network within a multilineage cVO. Transcriptomics, high-resolution 3D microscopy, and functional analyses showed that cVOs are similar to a human embryonic heart. The same vascular-inducing cocktail was then used to produce hVOs. CMs. cardiomyocytes: ECs. endothelial cells; SMCs, smooth muscle cells; PCs, pericytes; HCs, hepatocytes.



1038 Science 5 JUNE 2025

HUMAN DEVELOPMENT

Gastruloids enable modeling of the earliest stages of human cardiac and hepatic vascularization

Oscar J. Abilez^{1,2,3,4,5,6}*†, Huaxiao Yang^{1,7}†, Yuan Guan⁸, Mengcheng Shen¹, Zehra Yildirim¹, Yan Zhuge¹, Ravichandra Venkateshappa¹, Shane R. Zhao¹, Angello H. Gomez⁷, Marcel El-Mokahal⁷, Logan Dunkenberger^{1,4}, Yoshikazu Ono^{4,5}, Masafumi Shibata^{4,5}, Peter N. Nwokoye^{4,5}, Lei Tian¹, Kitchener D. Wilson^{1,9,10}, Evan H. Lyall¹⁰, Fangjun Jia¹, Hung Ta Wo¹, Gao Zhou^{11,12}, Bryan Aldana¹³, Ioannis Karakikes^{1,4}, Detlef Obal^{1,2,3,8}‡, Gary Peltz⁸, Christopher K. Zarins^{1,3,14}, Joseph C. Wu^{1,2,3,15,16}*

Although model organisms have provided insight into the earliest stages of cardiac and hepatic vascularization, we know very little about this process in humans because of ethical restrictions and the technical difficulty of obtaining embryos during very early development. In this study, we demonstrate that micropatterned human pluripotent stem cell—derived gastruloids enable in vitro modeling of the earliest stages of vascularization. We identify a combination of vascular-inducing factors that give rise to cardiac vascularized organoids with a spatially organized and branched vascular network. To show the broader utility of our vascularization strategy, we use the same vascular-inducing factors to produce hepatic vascularized organoids. Our results suggest that a conserved developmental program generates the vasculature within different types of organs.

Human pluripotent stem cells (hPSCs), including human embryonic stem cells (hESCs) and human induced pluripotent stem cells (hiPSCs), can differentiate into various cell types (1, 2), such as cardiomyocytes (CMs) (3), hepatocytes (HCs) (4) and individual types of cardiovascular cells (5), including endothelial cells (ECs) (6), smooth muscle cells (SMCs) (7, 8), pericytes (PCs) (9), fibroblasts (FBs) (10), endocardial cells (ENDOs) (11), and epicardial cells (EPIs) (12). Several approaches have been explored for achieving vascularization in organoids. For example, classic tissue engineering approaches have been used to generate vascularized cardiac (13-15) and hepatic (16) tissues using separately differentiated ECs and stromal cells. Forced overexpression of transcription factors ETV2, GATA6, and NGN1 have been used to induce EC formation in various types of organoids (17-19). Additionally, stereolithography and three-dimensional (3D) bioprinting have been used to produce vascular networks within hepatic and cardiac cell aggregates (20, 21). As an alternative method, de novo vascularization of kidney (22) and brain (23) organoids was achieved through in vivo implantation. Although self-organizing methods have been used to successfully create vascular organoids (24), both cardiac (25-35) and

Anesthesia, University of Iowa, Iowa City, IA, USA

hepatic (36) organoids generated with these approaches have variable levels of ECs, SMCs, and PCs; furthermore, whether these cell types form branched vasculature with lumina was not addressed because this was not the primary focus of these studies. Therefore, differentiating the key cell types of an organoid along with a de novo vasculature comprising robust branching, hierarchical organization, and lumina formation has not been fully achieved, highlighting a major bottleneck for organoid research (37–39).

Although model organisms have provided insight into the earliest stages of organ vascularization (40, 41), we know very little about this process in humans, owing to ethical restrictions and the technical difficulty of obtaining embryos at early developmental stages (42). Here, we used four hPSC fluorescent reporter systems and spatially micropatterned hPSCs (25, 43) to model the earliest developmental stages of cardiac and hepatic vascularization, which corresponds to the first 3 weeks of in vivo human development (Carnegie Stages 9 and 10) (44). We identified a growth factor and small molecule cocktail that when added to micropatterned hPSCs generated a spatially organized, branched, and lumenized vascular network within a multilineage cardiovascular organoid (cVO) comprising endocardial, myocardial, epicardial, and neuronal cell types, which are structurally and functionally similar to that of a 6.5-postconception week (PCW) human embryonic heart (Carnegie Stages 19 and 20) (45). To demonstrate the broader utility of this vascularization strategy, we used the same vascular-inducing cocktail to produce hepatic vascularized organoids (hVOs).

Results

Micropatterning of hPSCs results in spatially organized gastruloids, cardiovascular progenitors, and CMs

We and others have shown that geometric micropatterning of hPSCs enables reproducible and scalable formation of spatially organized germ layers (endoderm, mesoderm, and ectoderm) as gastruloids (46, 47), primitive streak (48, 49), CMs (25, 26, 43), and cardiac organoids (27). In each well of a multiwell plate, a single plasma-treated rubber stencil with a central hole was used to create 2-, 4-, or 6-mm circular hPSC monolayer micropatterns (Fig. 1A). Phase contrast (Fig. 1B and fig. S1A) and confocal fluorescence imaging (Fig. 1C) shows that the micropatterned hPSCs were pluripotent, with 2-mm micropatterns resulting in the most consistent formation of complete confluence and the highest ratio of CM-to-micropattern area. To provide an indication of the scale, a photograph shows 2-mm hPSC micropatterns (blue) in the center of four wells of a 48-well plate (Fig. 1D).

We confirmed that the total fluorescence area of pluripotency markers in the micropatterns was highly correlated with the number [coefficient of determination $(R^2)=0.99$] and theoretical total area $(R^2=0.99)$ of the micropatterns (fig. S1, B to D). Notably, validation of our method for quantification of the total fluorescence area was important for the screening experiments described below.

To vascularize cardiac organoids, we reasoned that we only needed to induce mesoderm from our hPSC micropatterns to simultaneously produce mesoderm-derived CMs, ECs, and SMCs as previously described (50). However, to vascularize endoderm-derived hepatic organoids, we would need to simultaneously induce endoderm to produce HCs, along with mesoderm to produce ECs and SMCs. Therefore, we used the hESC-RUES-GLR (germ layer reporter) cell

Science 5 JUNE 2025

¹Cardiovascular Institute, Stanford University, Stanford, CA, USA. ²Maternal and Child Health Research Institute, Stanford University, Stanford, CA, USA. ³Bio-X Program, Stanford University, Stanford, CA, USA. ⁴Department of Cardiothoracic Surgery, Stanford University, Stanford, CA, USA. ⁵Pediatric Cardiac Surgery, Stanford University, Stanford, CA, USA. ⁶Department of Biomedical Engineering, University of North Texas, Denton, TX, USA. ⁸Department of Anesthesia, Pain, and Perioperative Medicine, Stanford University, Stanford, CA, USA. ⁹Department of Parkology, Stanford University, Stanford, CA, USA. ¹⁰Rosebud Biosciences, Orinda, CA, USA. ¹¹Stanford Center for Genomics and Personalized Medicine, Stanford, CA, USA. ¹²Department of Genetics, Stanford University, Stanford, CA, USA. ¹⁴Department of Surgery, Stanford University, Stanford U

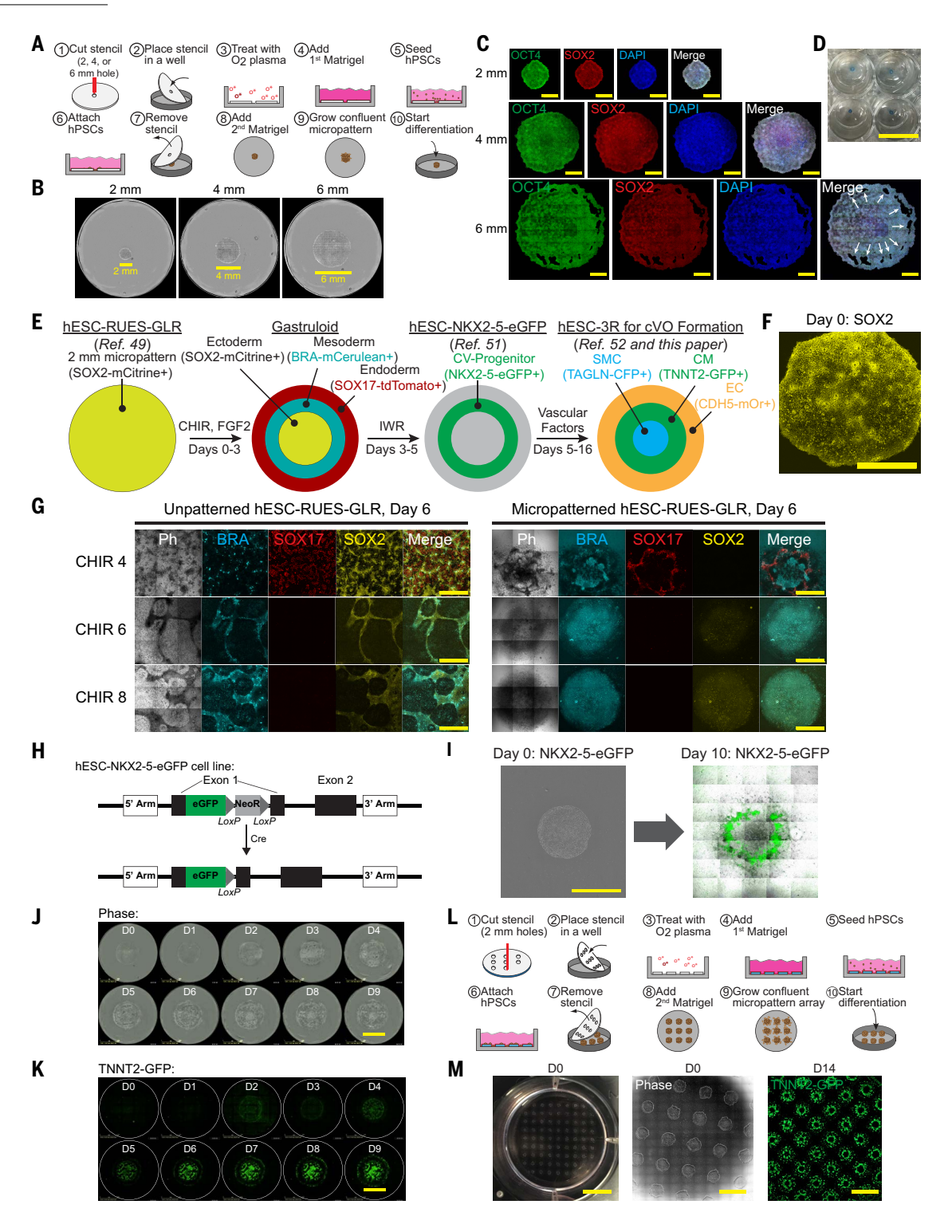


Fig. 1. Micropatterning of hPSCs results in spatially organized gastruloids, cardiovascular progenitors, and cardiomyocytes. (A) A single circular 2-, 4-, or 6-mm hPSC micropattern in each well of a multiwell plate is created from a silicone stencil. Differentiation begins when hPSC micropatterns are 100% confluent, typically at 2 to 3 days after seeding. (B) Phase imaging showing 2-, 4-, and 6-mm undifferentiated hPSC micropatterns. Scale bars, 2, 4, 6 mm, respectively. (C) Confocal imaging showing that 2-, 4-, and 6-mm hPSC micropatterns are pluripotent by immunostaining for OCT4 (green), SOX2 (red), and nuclear staining with 4′,6-diamidino-2-phenylindole (DAPI) (blue). White arrows show areas of incomplete hPSC confluence in 6-mm micropatterns. Scale bar, 1 mm. (D) Photograph showing 2-mm hPSC micropatterns (blue) in the centers of four wells of a 48-well dish. Scale bar, 9 mm. (E) The hESC-RUES-GLR (germ layer reporter) cell line (49) expresses SOX2, BRA, and SOX17 to identify undifferentiated cells and, upon differentiation, ectoderm, mesoderm, and endoderm arranged in stereotypical concentric rings as gastruloids. The hESC-NKX2-5-eGFP cell line (51) identifies cardiovascular progenitors in the middle ring arising from mesoderm. The hESC-3R cell line [(52) and this paper] identifies CMs, SMCs, and ECs arising from cardiovascular progenitors. (F) Confocal imaging at day 0 showing SOX2 expression throughout a single undifferentiated micropattern. Scale bar, 1 mm. (G) Confocal imaging showing unpatterned (left) and micropatterned (right) RUES-GLR hESCs at day 6 with CHIR 4, 6, and 8 μM added at day 0. Unpatterned hESCs give rise to disorganized germ layers (BRA+, SOX17+, SOX2+ expression), and SOX2 is expressed at all CHIR concentrations. By contrast, micropatterned hESCs give rise to organized germ layers with minimal SOX2 expression. For

Science 5 JUNE 2025 2 of 22

CHIR 4 µM, micropatterned hESCs give rise to a BRA⁺ mesodermal central area surrounded by a SOX17⁺ endodermal ring, with no SOX2 ectodermal expression. Scale bar, 1 mm. (**H**) The hESC-NKX2-5-eGFP cell line expresses eGFP under the cardiovascular progenitor transcription factor NKX2-5, as previously described (51). (**I**) A single NKX2-5-eGFP micropattern at day 0 (left) differentiated over 10 days showing organized ring formation of eGFP⁺ cardiovascular progenitors leading to beating CMs (right). Scale bar, 2 mm. (**J**) Phase imaging showing CM differentiation of a 6-mm hESC-TNNT2-GFP micropattern from day 0 to 9 (D0 to D9). Scale bar, 6 mm. (**K**) Fluorescence imaging of (J) showing GFP⁺ CMs (green). Scale bar, 6 mm. (**L**) An array of circular 2-mm hPSC micropatterns in each well of a multiwell plate is created from a silicone stencil. For a 6-well dish, up to 77 hPSC micropatterns can be created per well for a total of 462 micropatterns. (**M**) (Left) Photograph showing an array of 77 hPSC micropatterns in 1 well of a 6-well dish; (middle) phase imaging showing undifferentiated hPSC micropatterns; and (right) fluorescence imaging showing organized and arrayed GFP⁺ CMs. Scale bars, 10, 4, and 4 mm, respectively.

line (49) (Fig. 1, E and F, and fig. S2A) to visualize germ layer formation in the presence of different concentrations of a GSK3 β inhibitor (CHIR-99021, CHIR) in unpatterned versus micropatterned hPSCs.

Whereas unpatterned RUES-GLR hESCs at day 6 gave rise to disorganized germ layers at different CHIR concentrations, the micropatterned group consistently generated organized germ layers (Fig. 1G). After 4 μ M of CHIR induction, a central BRA⁺ mesodermal area was surrounded by a SOX17⁺ endodermal ring, whereas SOX2⁺ ectoderm was absent. By contrast, SOX2 was expressed in the unpatterned group at all CHIR concentrations in a disorganized fashion. Immunostaining of BRA and SOX17 confirmed the reporter expression seen in the CHIR 4- μ M micropattern group (fig. S2B).

Arrays of micropatterned RUES-GLR hESCs differentiated under the same conditions as single micropatterns also showed centrally located BRA⁺ expression surrounded by maximum SOX17⁺ expression, peaking at day 11 for both conditions (fig. S2, C and D). Thus, single and arrayed micropatterns gave rise to similar BRA and SOX17 temporal and spatial expression that was different from the unpatterned group.

Next, we used the hESC-NKX2-5-eGFP (eGFP, enhanced green fluorescent protein) cell line (51) (Fig. 1H) to visualize the effects of micropatterning on cardiovascular progenitor formation. Using our baseline CM differentiation protocol (see supplementary materials), we showed that single NKX2-5-eGFP micropatterns differentiated over 10 days gave rise to NKX2-5-eGFP⁺ cardiovascular progenitors in an organized, ring-shaped morphology, leading to beating CMs (Fig. 1I and movie S1). Using an hESC-TNNT2-GFP fluorescent reporter line (52), we showed that 6-mm micropatterns could be differentiated into CMs (Fig. 1, J and K) and that the progression of this differentiation could be tracked in situ over a course of 9 days (movie S2). At this juncture, using three fluorescent hPSC reporter lines (hESC-RUES-GLR, hESC-NKX2-5-eGFP, and hESC-TNNT2-GFP), we demonstrated that micropatterning gave rise to organized germ layers, cardiovascular progenitors, and CMs, thus providing a foundation for screening conditions for cVO formation.

To scale up micropattern formation, a single plasma-treated rubber stencil with an array of 2-mm holes was used to create arrayed hPSC micropatterns. For a 6-well plate, up to 77 micropatterns (7 by 7 array + 7 by 2 columns + 7 by 2 rows) could be created per well for a total of 462 micropatterns resulting in 462 GFP⁺ CM colonies (Fig. 1, L and M).

Creation of a triple reporter line enables optimization of differentiation conditions leading to cVO formation

To facilitate the screening of various differentiation conditions for cVO formation, we next created a hESC triple reporter line (hESCTNNT2-GFP/CDH5-mOrange/TAGLN-CFP) (hESC-3R) comprising the TNNT2 (troponin-T) promoter-driven GFP to identify CMs, the CDH5 (VE-cadherin) promoter-driven mOrange to identify ECs, and the TAGLN (SM22 α) promoter-driven cyan fluorescent protein (CFP) to identify SMCs (Fig. 2A). Two lentiviral vectors, one for the CDH5 promoter-driven mOrange and the other for the TAGLN promoter-driven CFP (fig. S2, E to H), were transduced into an hESC-TNNT2-GFP fluorescent reporter line (52), and the pluripotency of two polyclonal and six monoclonal lines was confirmed (fig. S2, I to K). Using differentiation protocols specific for CMs (3), ECs (53), and SMCs (7, 8), we observed an overlay of fluorescent signals between endogenously

expressed tags and antibody-based staining of cell type – specific markers in the hESC-3R line (Fig. 2B).

Next, we tested the effects of different CHIR concentrations (3, 4, and 5 $\mu\text{M})$ combined with vascular endothelial growth factor (VEGF) (50 ng/ml) on CM and EC codifferentiation over 14 days using the hESC-3R line. hESC-3R micropatterns treated with CHIR + fibroblast growth factor 2 (FGF2) + IWR-1 (IWR) (Control) differentiated to CMs at 5 μM CHIR along with a few ECs at all concentrations in the absence of VEGF (fig. S3A). By contrast, hESC-3R micropatterns treated with 5 μM CHIR and 50 ng/ml VEGF at days 6, 8, 10, and 12 of differentiation gave rise to the most CMs and ECs (fig. S3B). These initial results were the basis for additional screening conditions to fine-tune the optimal codifferentiation condition to create cVOs.

A schematic shows the timeline, stages, cell types, geometry, media, and growth factors for creating CMs, ECs, SMCs, and cVOs (Fig. 2C). Our strategy for codifferentiation was to first create a cardiovascular (CV) progenitor pool and then to add additional small molecules and growth factors to facilitate optimal codifferentiation of CMs, ECs, and SMCs to produce cVOs (fig. S3C). We used previously established methods for guiding concentrations and timing to achieve low and high production of CMs (3, 14, 50), ECs (6, 14, 54–56), and SMCs (7, 57) (fig. S3D).

A total of 34 screening conditions (n=4 to 6 per micropattern per condition, 175 total micropatterns) were tested to differentiate hESC-3R micropatterns to CMs, ECs, and SMCs as eVOs (table S1 and fig. S3E). CHIR 4 μ M was used in odd-numbered conditions (n=88 micropatterns) and CHIR 5 μ M in even-numbered conditions (n=87 micropatterns) (fig. S3F). Overall, CHIR 5 μ M gave rise to significantly more CMs (***P<0.0005), ECs (***P<0.0005), and SMCs (***P<0.0005) compared with CHIR 4 μ M for each condition (fig. S3G and movie S3).

Condition 32, which produced eVOs with the most CMs, ECs, and SMCs (Fig. 2, D and E, Fig. 3, A to L, and fig. S3, H to J), consists of the following stage-specific differentiation small molecules and growth factors: CHIR, 5 μ M (day 0); FGF2, 5 ng/ml (days 0, 7, 9, 11, 13, 15); IWR, 5 μ M (day 3); VEGF, 50 ng/ml (days 5, 7, 9, 11, 13, 15); SB431542 (SB), 10 μ M (days 7, 9, 11); angiopoietin-2 (ANG2), 50 ng/ml (days 5, 7); angiopoietin-1 (ANG1), 50 ng/ml (days 9, 11); platelet-derived growth factor BB (PDGF-BB), 10 ng/ml (days 7, 9, 11, 13, 15); and transforming growth factor- β 1 (TGF- β 1), 2 ng/ml (days 13, 15). Condition 2 (Control) was the baseline CM differentiation condition with only CHIR, FGF2, and IWR being used.

Time-lapse imaging showed more CM, EC, and SMC formation in Condition 32 compared with Control (Fig. 2, D and E). Time-course CM formation for Control (n=4) and Condition 32 (n=6) showed that CMs emerged around day 8 for both conditions (Fig. 3, A and B), and by day 12, there were significantly more CMs in Condition 32 (***P < 0.0005) (Fig. 3, C and D). Time-lapse imaging showed that ECs were already present at day 3 for both conditions and that their formation began to increase around day 5 for Condition 32, a few days before CM formation (Fig. 3, E and F); by day 12, there were significantly more ECs in Condition 32 (***P < 0.0005) (Fig. 3, G and H). SMCs began to increase around day 8 for Condition 32 (Fig. 3, I to J), and by day 12, there were significantly more SMCs in Condition 32 (***P < 0.0005) (Fig. 3, K and L).

As noted above, the rates of EC and CM formation increased around days 5 and 8, respectively (fig. S3K). In terms of vascularization factor cross-talk with ECs and CMs, at day 12, VEGF alone generated the most

Science 5 JUNE 2025 3 of 22

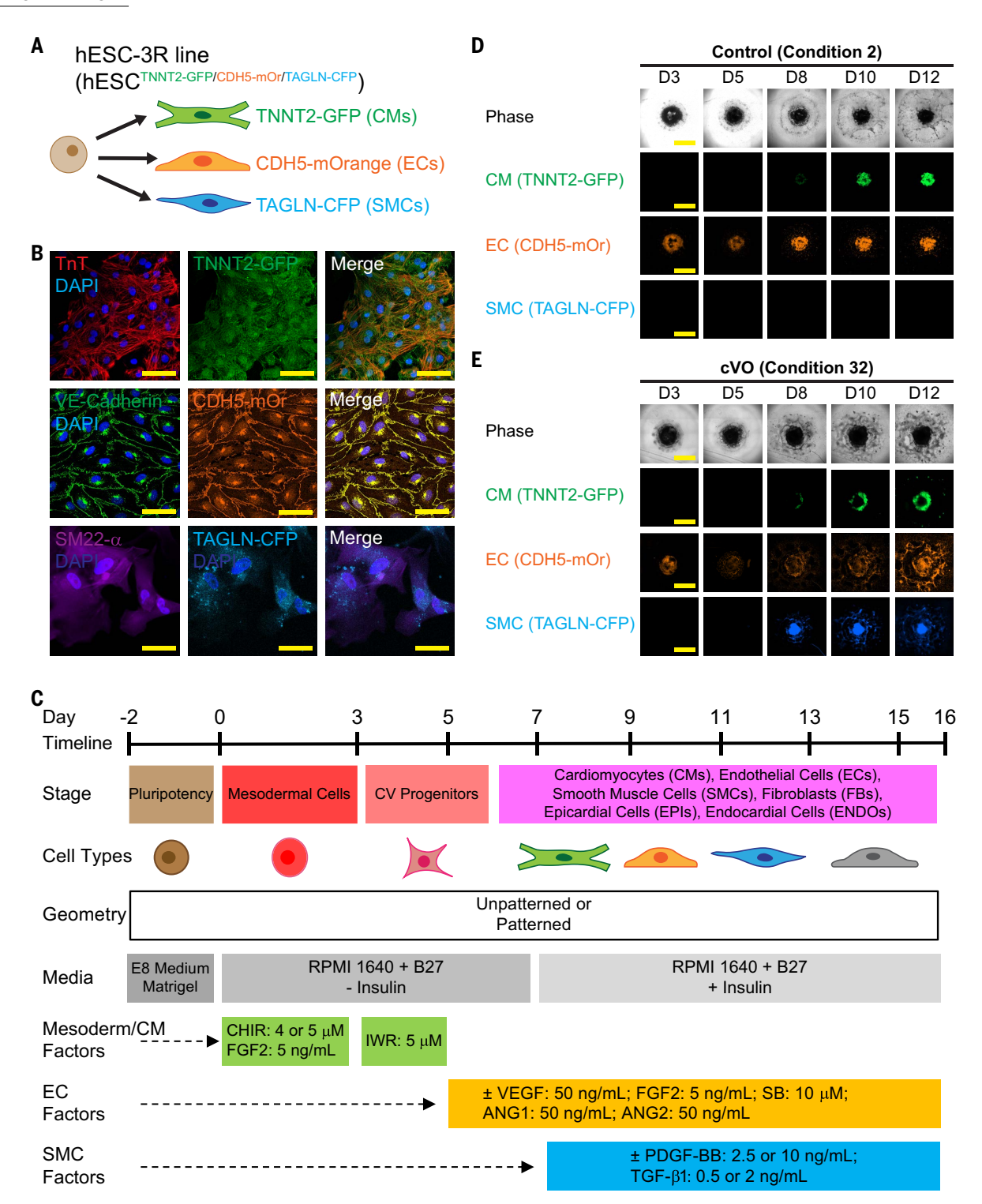
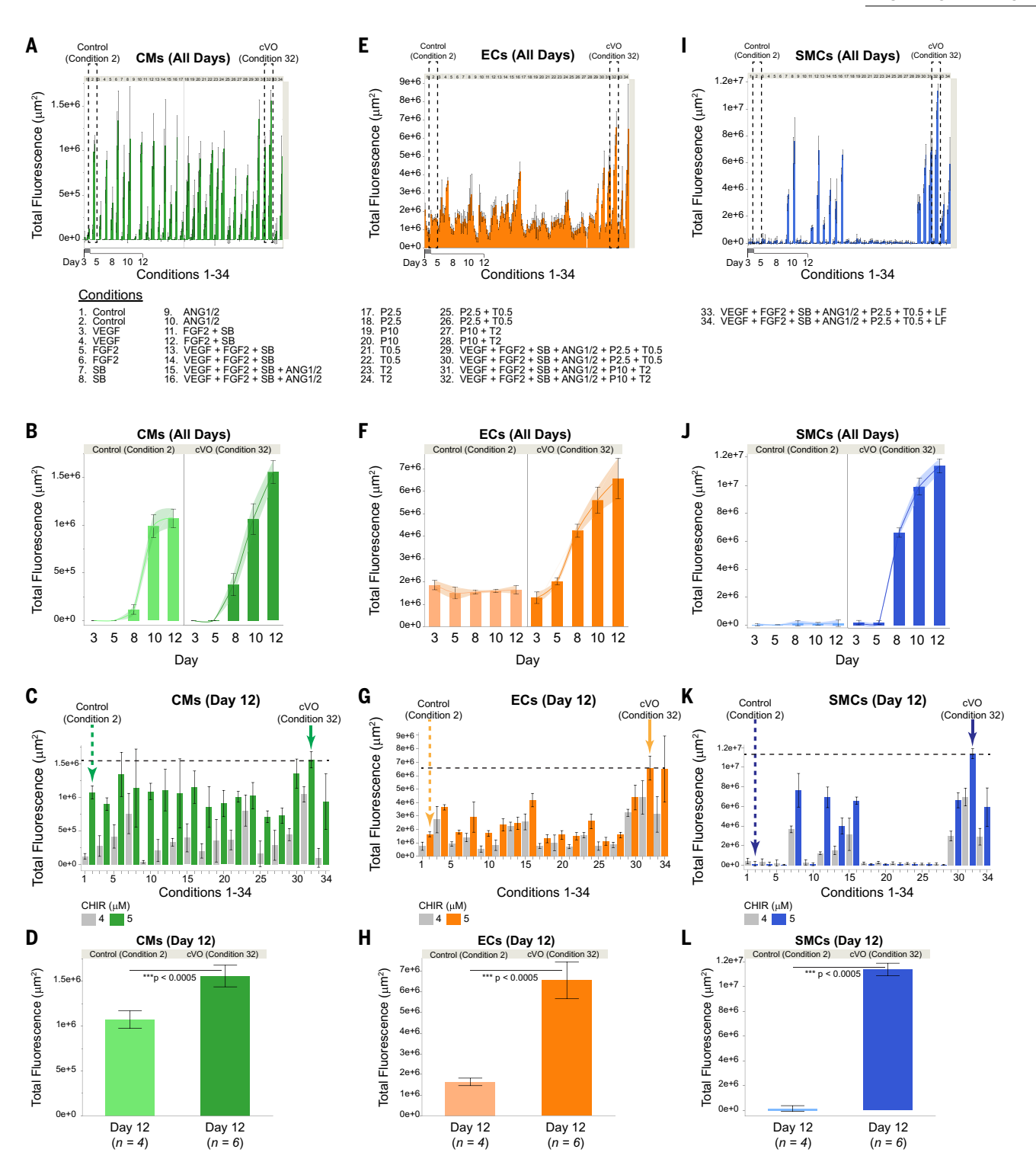


Fig. 2. Creation of a triple reporter line enables screening differentiation conditions leading to cVO formation. (A) The hESC-3R line comprises the TNNT2 (troponin-T) promoter driving GFP to identify CMs, the CDH5 (VE-cadherin) promoter driving mOrange to identify ECs, and the TAGLN (SM22α) promoter driving cyan fluorescent protein (CFP) to identify SMCs. (B) Confocal fluorescence imaging and immunostaining confirms the differentiation of hESC-3R into CMs (coexpression of troponin-T (TnT) with TNNT2-GFP) (top row), ECs (coexpression of VE-cadherin with CDH5-mOrange) (middle row), and SMCs (coexpression of SM22α with TAGLN-CFP) (bottom row). Nuclei are stained with DAPI. Scale bar, 50 μm. (C) Schematic showing timeline, stage, cell types, geometry, media, and growth factors for codifferentiating CMs, ECs, and SMCs, leading to formation of cVOs. (D) Representative time-lapse imaging shows CM, EC, and SMC formation over 12 days for Control (Condition 2). (E) Representative time-lapse imaging shows CM, EC, and SMC formation over 12 days for cVO (Condition 32). In the cVO sample, note ring formation of CMs, with outward radiation of ECs, and central SMCs. Scale bar, 2 mm. Condition 2 (Control) is the standard cardiomyocyte differentiation with only the factors CHIR, FGF2, and IWR. Condition 32 (cVO) consists of the following small molecules and growth factors: CHIR, 5 μM (day 0); FGF2, 5 ng/ml (days 0, 7, 9, 11, 13, 15); IWR, 5 μM (day 3); VEGF, 50 ng/ml (days 5, 7, 9, 11, 13, 15); SB, 10 μM (days 7, 9, 11); ANG2, 50 ng/ml (days 5, 7); ANG1, 50 ng/ml (days 9, 11); PDGF-BB, 10 ng/ml (days 7, 9, 11, 13, 15); and TGF-β1, 2 ng/ml (days 13, 15).

Science 5 JUNE 2025 4 of 22



Science 5 JUNE 2025 5 of 22

ECs compared with Control (n=10, ***P<0.0005), with FGF2 alone (n=10, ***P<0.0005), and SB alone (n=8, *P<0.05), without significant differences in CM formation (fig. S3, L and M). The combination of FGF2, SB, and VEGF, along with the angiopoietins, produced the most ECs in Condition 32. For arrays of hESC-3R micropatterns, Condition 32 also gave rise to all the three cell types (fig. S3N).

cVOs comprise myocardial, vascular, endocardial, epicardial, and neuronal cell types

After we extended the differentiation of cVOs from 12 to 16 days (equivalent to ~3 weeks of in vivo human development), CMs, SMCs, and branching ECs arranged in a concentric fashion (Fig. 4, A and B; fig. S4A; and movie S4). Imaris software –enabled 3D surface renderings of hESC-3R micropatterns and cVOs showed that cVOs developed significantly in the z axis (~300 μ m versus ~30 μ m, ***P < 0.0005) and volumetrically (~2.5-fold, **P < 0.005) (Fig. 4C). We confirmed that CMs coexpressed troponin-T (TnT) and TNNT2-GFP, ECs coexpressed CD31 and CDH5-mOrange, and SMCs coexpressed calponin and TAGLN-CFP (Fig. 4, D to F). Compared with hESC-3R micropatterns, unpatterned hESC-3R cells resulted in unorganized and random distribution of CMs and ECs (fig. S4B).

cVOs contained branched ECs intimately surrounding CMs and SMCs and moved in unison together with each CM contraction (fig. S4C and movie S5). SMCs also coexpressed SMA and TAGLN-CFP (fig. S4D). Arrays of hESC-3R micropatterns also differentiated into cVOs and contained CMs, SMCs, and branched ECs arranged in a concentric fashion (Fig. 4, G and H). Individual micropatterns gave rise to independent patterns of cVOs despite sharing the same media.

To demonstrate increased throughput without using stencils, we used the same micropattern monolayer ("2D") differentiation protocol for cVOs to create more spherical "3D" cVOs over 14 days under a range of CHIR at higher concentrations (6.0 to 8.5 μ M) on a single hESC-3R colony formed in each well of a 96-well plate. CHIR 7.0 μ M generated the most CMs and ECs, with CM and EC formation being inversely related across all concentrations (fig. S4E). The higher CHIR needed in this format was expected as a result of gradient dilution in the core of 3D cVOs. We validated our vascularization protocol with an hiPSC line (SCVI 113, Stanford CVI Biobank) and confirmed the presence of CMs, ECs, and SMCs within hiPSC-derived cVOs (fig. S4, F and G). Using another method to create "3D" cVOs, we adapted our "2D" differentiation protocol to a "2D-to-3D" protocol recently used to create multichamber cardioids (34) and obtained robust vascularization (fig. S4H).

We next performed temporal bulk RNA-sequencing (bRNA-seq) on (i) single undifferentiated micropatterned hESC-3R colonies, (ii) Controls (baseline cardiac differentiation, with no vascularization factors added), and (iii) cVOs (n=3 for all groups). Weighted gene coexpression network analysis (WGCNA) showed clustering of pluripotency, mesoderm, CV progenitor, CM, EC, SMC, FB, and vascularization genes over 16 days. Vascularization genes were the highest in cVOs and peaked at day 16 (Fig. 4I). Principal component analysis (PCA) showed developmental differences between all three groups over 16 days. The divergence between Control and cVO groups emerged at day 5, when vascular induction began (fig. S4I).

From our bRNA-seq analysis, we compared Control and cVO groups for selected gene groups as follows: CM, EC, SMC/PC, and NOTCH-DELTA-JAG groups (Fig. 4J) along with pluripotent, mesoderm/CV progenitor, FB, and EPI groups (fig. S4J). CM genes were higher for Controls compared with cVOs; for EC and NOTCH-DELTA-JAG genes, the divergence of expression between Controls and cVOs began around day 5, when vascular specifying factors were added to the cultures; and SMC/PC genes generally increased for both groups (Fig. 4J). As expected, pluripotency genes decreased, and mesoderm/CV progenitor genes peaked early in differentiation in both Controls and cVOs; by contrast, FB genes for both groups increased (fig. S4J). The EPI genes WTI and TBX18 were higher and the same, respectively, in cVOs compared with Controls,

whereas *UPK3B* and *ANXA8* genes were lower in cVOs, suggesting a mixed population of EPI cells in cVOs (fig. S4J).

For cVOs, we also found a multitude of up-regulated genes from our bRNA-seq analyses related to cardiogenesis and vascularization in mesoderm/CV progenitor, atrial, ventricular, adrenergic, endothelial, arterial, venous, and endocardial cells, bone morphogenic protein (BMP) pathway, TGFβ pathway, VEGF pathway, WNT pathway, PDGF pathway, angiopoietin, gap junction, and paracrine gene groups (fig. S5, A to M, green: CM-related; orange: EC-related; blue: SMC-related; red: all other gene groups). Notably, we found that several members of the angiopoietin family, including *ANGPT2*, *ANGPTL1*, *ANGPTL4*, *ANGPTL6*, and *TIE1* were all up-regulated in cVOs, which is consistent with their established role in vascularization (56, 58, 59).

Ingenuity pathway analysis (IPA) showed up-regulated canonical pathways also known to be important in cardiovascular development, including epithelial-to-mesenchymal transition (EMT), HIF1α signaling, and HOTAIR signaling (fig. S6A). IPA comparing Controls to cVOs from days 2 to 16 also showed up-regulated upstream regulators known to be important in cardiovascular development, including *PDGFBB*, *TGFB1*, *CD36*, *BMP4*, *VEGFA*, *FGF2*, and *HIF1A* (fig. S6B). Furthermore, IPA showed that the NOTCH pathway was up-regulated in cVOs compared with Controls (fig. S6C), whereas the BMP pathway was up-regulated in both groups (fig. S6D).

IPA of the WGCNA dark gray module within the "Cardiomyocyte/ Endothelial/Smooth Muscle/Fibroblast Genes" cluster in Fig. 4I confirmed a cardiogenesis regulator effect network with upstream regulators including *BMP*, $TGF\beta$, and *WNT11* activating downstream genes including MEF2C, NKX2-5, TBX5, MYH6, and NPPA, leading to cardiogenesis (fig. S6E). IPA of the WGCNA pale turquoise module within the "Vascularization Genes" cluster in Fig. 4I confirmed a vascularization regulator effect network with upstream regulators including VEGF, CD36, JAG2, and JUNB, which activate genes such as PDGFB, FLT1, MMP9, TGFβ1, HIF1A, FN1, and DLL4, leading to downstream vascularization functions (fig. S6F). IPA of day 16 cVOs versus Controls showed up-regulated vascularization functions (fig. S6G) and a VEGF regulator effect network on ITGA1, MMP9, CDH5, F3, NOTCH4, CD34, and DLL4, leading to downstream development of vasculature (fig. S6H). IPA also showed up-regulated vascularization functions, including angiogenesis and vasculogenesis (fig. S6I). Up-regulation over time generally began to increase at day 8, after vascularization factors were added in cultures at day 5. IPA of day 16 cVOs versus Controls showed upregulation of vascularization functions (fig. S6J).

To obtain higher cellular resolution within cVOs, we next performed single-cell RNA-sequencing (scRNA-seq) of three cVO samples (day 16) and then downstream integrative analysis using Seurat (60) with a 6.5-PCW (~45 days) human embryonic heart (Carnegie Stages 19 and 20) from a recent study (45) that was previously reanalyzed by our group (61).

Cluster annotation with the Azimuth human adult heart scRNA-seq reference set (62–64) (table S2) (https://azimuth.hubmapconsortium. org/), a web application developed as part of the NIH Human Biomolecular Atlas Project (HuBMAP) (https://commonfund.nih.gov/hubmap) revealed multiple myocardial, vascular, endocardial, epicardial, and neuronal cell types in cVOs and the 6.5-PCW heart (Fig. 4K; fig. S7, A to F; and fig. S8, A to F).

cVOs showed shared subtypes of CMs, ECs, and SMCs with the 6.5-PCW heart (fig. S9, A to C). Expression of representative atrial (*MYH6* and *MYL7*) and ventricular (*MYH7* and *MYL2*) CM genes was generally higher for the 6.5-PCW heart compared with cVOs (fig. S9D). Expression of representative arterial (*CXCR4*), venous (*EPHB4*), capillary (*FLT1*), endocardial (*NFATC1*), and lymphatic (*MMRN1*) EC genes was generally lower for the 6.5-PCW heart compared with cVOs (fig. S9E). As in the original analysis by Asp *et al.* (45), a venous EC subtype was not identified in the 6.5-PCW heart in our integrated analysis. Expression of representative SMC (*TAGLN* and *ACTA2*) and PC (*PDGFRB* and

Science 5 JUNE 2025 6 of 22

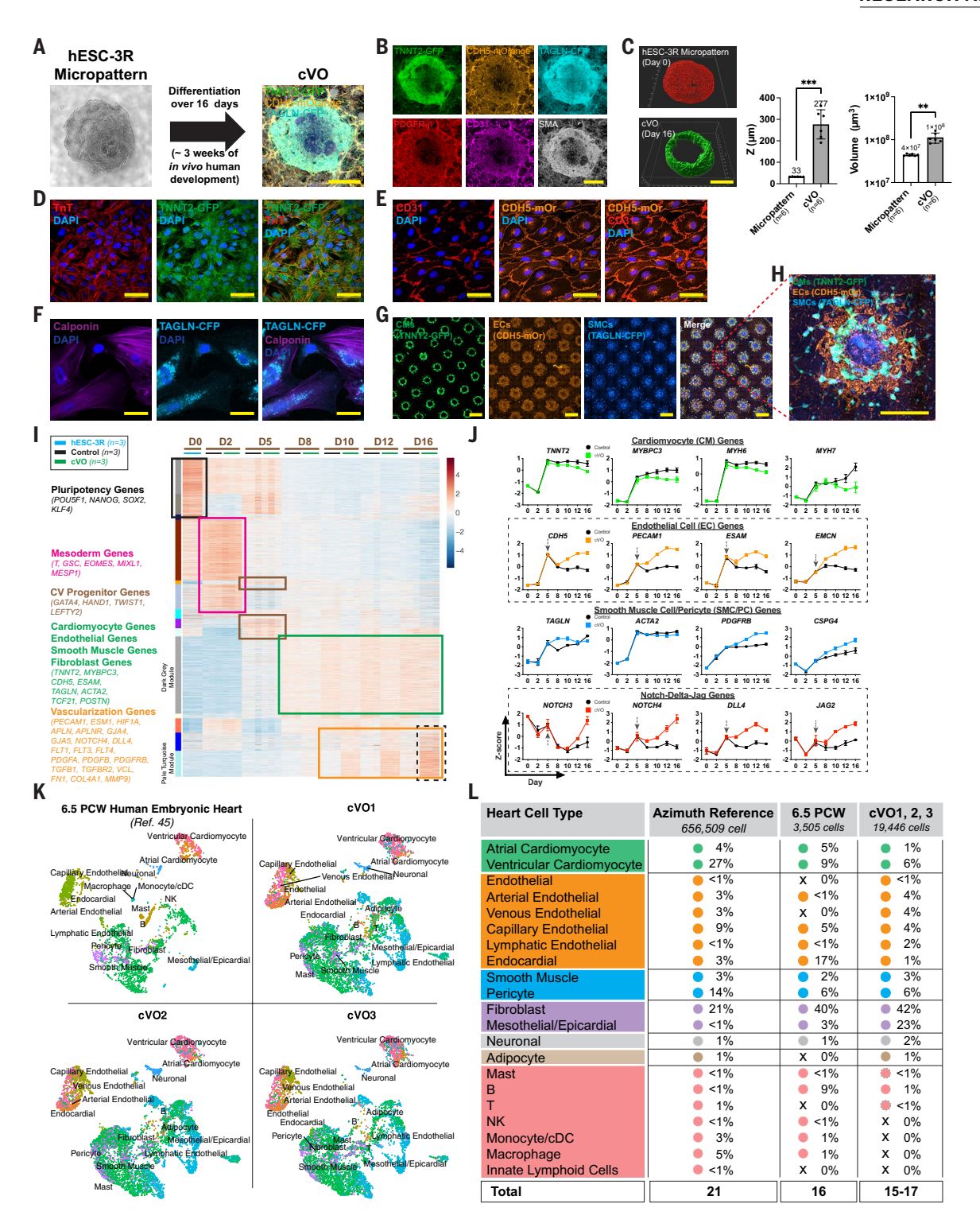


Fig. 4. cVOs comprise multiple myocardial, vascular, endocardial, epicardial, and neuronal cell types. (A) Phase (left) and maximum intensity projection (MIP) confocal imaging (right) shows the differentiation of a single hESC-3R micropattern over 16 days (~3 weeks of invivo human development) into a cVO containing CMs (green), ECs (orange), and SMCs (blue). Note concentric organization of cell types and EC branching. Scale bar, 0.5 mm. (B) Individual channels showing CMs (TNNT2-GFP), ECs (CDH5-mOrange and CD31), SMCs (TAGLN-CFP and SMA), and PCs (PDGFR-β). Scale bar, 0.5 mm. (C) 3D surface renderings of hESC-3R micropatterns and cVOs show that cVOs develop significantly in the z axis (~300 μm versus ~30 μm, ***P < 0.0005) and volumetrically (~2.5-fold, **P < 0.005). Scale bar, 0.5 mm. (D) Confocal fluorescence images showing that hESC-3R CMs coexpress troponin-T (TnT) (red) with TNNT2-GFP (green). Nuclei are labeled with DAPI (blue). Scale bar, 50 μm. (E) Confocal fluorescence images showing that hESC-3R ECs coexpress CD31 (red) with CDH5-mOrange (orange). Nuclei are labeled with DAPI (blue). Scale bar, 50 μm. (F) Confocal fluorescence images showing that hESC-3R SMCs coexpress calponin (purple) with TAGLN-CFP (cyan). Nuclei are labeled with DAPI (blue). Scale bar, 50 μm. (G) Fluorescence imaging shows an array of hESC-3R micropatterns differentiated over 16 days into cVOs containing concentrically self-organized CMs (green), ECs (orange), and SMCs (blue). Note that individual micropatterns give rise to an array of independently formed cVOs despite sharing the same media. Scale bar, 2 mm. (H) Enlarged area from red box in (G) showing concentric organization of CMs, ECs, and SMCs, with EC branching. Scale bar, 1 mm. (I) Temporal bRNA-seq was performed for undifferentiated hESC-3R micropatterns (blue, n = 3),

Science 5 JUNE 2025 7 of 22

RESEARCH ARTICLE

Control differentiation (black, n = 3), and cVO differentiation (green, n = 3). Weighted gene coexpression network analysis (WGCNA) heat map shows clusters of pluripotency, mesoderm, CV progenitor, cardiomyocyte, endothelial, smooth muscle, fibroblast, and vascularization genes over 16 days (D0-16). Note up-regulated vascularization genes in D16 cVOs (black dashed rectangle). (J) Comparison of CM, EC, SMC/PC, and Notch-Delta-Jag gene groups from bRNA-seq most notably show that EC and Notch-Delta-Jag gene expression (dashed black rectangles) is higher for cVOs and diverges from Controls around day 5 (dashed arrows), when vascular-inducing factors are added to the cultures. (K) scRNA-seq of three cVOs (day 16) integrated with a 6.5-PCW human embryonic heart dataset (45); cluster annotation with the Azimuth adult heart reference dataset reveals myocardial, vascular, endocardial, epicardial, and neuronal cell types in cVOs. (L) cVOs and a 6.5-postconception week (PCW) heart comprise 15 to 17 and 16 heart cell types, respectively, of the 21 types annotated in the Azimuth adult heart reference. Percentages of each cell type are listed for each group, with fibroblasts and mesothelial/epicardial types accounting for the most cVO cell types. Hematopoietic cell types are least represented in cVOs compared with the other two groups. NK, natural killer cell.

CSPG4) genes was generally higher for the 6.5-PCW heart compared with cVOs (fig. S9F). Compared with the Azimuth adult heart and the 6.5-PCW heart, cVOs comprised fewer CMs, ECs, and SMCs/PCs (fig. S9G). Furthermore, as a result of fewer CMs, cVOs had a higher EC:CM ratio than the adult and 6.5-PCW hearts; cVOs also had an intermediate EC:SMC/PC ratio compared with the adult and 6.5-PCW hearts because they were affected by having slightly more SMCs/PCs and fewer ECs than the 6.5-PCW heart. Lastly, cVOs had the lowest CM:SMC/PC ratio, mostly because of fewer CMs compared with the other two groups (fig. S9G).

cVOs and the 6.5-PCW heart comprised 15 to 17 and 16 heart cell types, respectively, of the 21 types that are annotated in the Azimuth adult heart reference. Fibroblasts and mesothelial/epicardial types accounted for the most cVO cell types, whereas hematopoietic cell types were least represented in cVOs compared with the other two groups (Fig. 4L and table S3). The 6.5-PCW heart is the earliest in vivo scRNA-seq dataset to date but is still \sim 3.5 weeks older than our cVOs; thus, we expected that our cVOs would not have all the cell types found in the 6.5-PCW heart or the Azimuth adult heart reference.

cVOs comprise branched and lumenized vasculature spatially integrated with atrial, ventricular, endocardial, epicardial, and neuronal cell types

To further characterize myocardial, vascular, endocardial, epicardial, and neuronal cell types within cVOs, we used maximum intensity projection (MIP) confocal imaging and Imaris software-enabled 3D surface rendering of various cell type-specific markers. cVOs comprised CD31⁺ EC branches surrounded by PDGFR- β ⁺ PCs that integrated with and penetrated TNNT2-GFP⁺ CMs (Fig. 5A) along with SM22α⁺ SMCs surrounding branched ECs (Fig. 5B and movie S6). Imaris 3D surface rendering of the cVO seen in Fig. 5A shows a network of ECs integrated with the CM ring (Fig. 5C), where ECs form vascular branches ranging from 4 to 40 μm in diameter (Fig. 5D and fig. S10A). Vascular branch length (min-max, 2 to 201 μ m), diameter (min-max, 3 to 40 μ m), total length (1.7 \times 10⁵ μ m), and total volumes (1.8 \times 10⁷ μ m³) (Fig. 5E) were consistent with a microvasculature phenotype and within the range of values recently reported for 3D quantification of vascular characteristics (65). Imaris 3D surface rendering showed ECs within a cVO forming branches with three lumina of approximately 20 µm in diameter (Fig. 5F). To confirm lumen formation, we performed confocal imaging showing CMs, branched ECs, and 1-µm-diameter crimson microspheres contained within EC branches (Fig. 5G); we also showed lumen formation with smaller 0.2-µm far-red microspheres (pseudocolored white) at a lower magnification (fig. S10B and B') to account for any spectral overlap with the CDH5-mOrange signal.

An Imaris 3D surface rendering showed PDGFR- β^+ PCs surrounding branched CD31⁺ ECs within TNNT2-GFP⁺ CMs (Fig. 5H). High-magnification (63×) and high-resolution 3D confocal imaging showed ECs forming ~10-µm diameter lumen outside and inside CM areas; wheat germ agglutinin (WGA) staining of cellular plasma membranes also confirmed lumen formation (Fig. 5, I to K, and movie S7). We also observed small nucleated nonattached cells within the lumen. Lastly, we showed 1-µm-diameter blue microspheres moving within a lumen in sync with each cVO contraction (movie S8), demonstrating true lumen formation.

The presence of PCs was also confirmed by NG2/CSPG4 and GATA4 labeling (fig. S10, C and D). MIP confocal images showed an inner ring of NFATC1⁺ ENDOs surrounded by an outer ring of CMs and integrated with ECs (Fig. 6A). WT1⁺/TBX18⁺ (Fig. 6B and fig. S10E) EPIs were identified within the cVO center and in close proximity to CMs and ECs. DDR2⁺, DCN⁺, and LUM⁺ fibroblasts were also interspersed with MYH6⁺/TNNT2-GFP⁺ CMs and CD31⁺ ECs (Fig. 6C and fig. S10, F and G). Lastly, we identified β -Tubulin III⁺ neuronal cells interspersed with CMs and ECs (Fig. 6D).

To examine the cardiogenic and vascularization potential of cVOs from hiPSCs, we conducted differentiation on five randomized hiPSC lines derived from donor individuals representing different sexes, races, and ethnicities (table S4). cVOs had significantly more ECs (**P < 0.005, ***P < 0.0005, ***P < 0.0005) compared with Controls for each line while maintaining similar amounts of CMs (fig. S11, A to C).

cVOs beat slower and have longer electrical, calcium, and contraction durations than Controls as shown by multiple functional assessments

To functionally characterize our cVOs, we used multielectrode array (MEA) electrophysiology (EP), sharp electrode EP, calcium transient analysis, contraction analysis, and nitric oxide (NO) testing. MEA EP showed that cVOs beat significantly slower than Controls (*P < 0.05) (~50 versus ~70 beats/min) without a significant difference in spike amplitude (Fig. 6, E and F, and fig. S12A). These beat rates are similar to rates from in vitro cultured human fetal cardiac tissue (~60 beats/ min) and day 12 hPSC-derived CMs (~50 beats/min) (66). Moreover, more than 3 weeks of intense in vitro electromechanical (EM) conditioning of engineered cardiac tissue (ECT) made from the day 12 hPSCderived CMs was necessary to increase rates up to \sim 140 beats/min (66). This suggests that EM conditioning may be required to achieve cVO beat rates that mimic average in vivo fetal heart rates of ~145 beats/min (67). Sharp electrode EP showed that corrected action potential duration at 90% repolarization (APD90c) was significantly higher in cVO ventricular-like CMs compared with Control (*P < 0.05) but not significantly different for atrial-like CMs (Fig. 6, G and H). Additionally, sharp electrode EP showed increased maximum upstroke velocity (Vmax) of Control ventricular-like CMs compared with Control atriallike CMs, as well as increased APD90c of cVO ventricular-like CMs compared with cVO atrial-like CMs. All other atrial-atrial, ventricularventricular, and atrial-ventricular, intercomparisons (Ctrl versus cVO), and intracomparisons (Ctrl versus Ctrl and cVO versus cVO) showed no significant differences (fig. S12B). Sharp electrode EP data revealed that analyzed cVOs comprised more atrial-like and less ventricular-like CMs compared with Control (Fig. 6I).

Calcium transient analysis showed that cVOs had increased peak calcium, CDT30, CDT50, CDT90, and Tau (all ****P < 0.00005), and decreased max rise slope (*P < 0.05), compared with Controls (fig. S12C and movie S9). Contraction transient analysis showed that cVOs had significantly decreased beat rates (****P < 0.00005) and contraction amplitude (****P < 0.00005), along with increased time-to-peak (*P < 0.05), contraction duration (****P < 0.00005), and relaxation time (****P < 0.00005), compared to Controls. The beat rates of cVOs showed less variability than Controls (fig. S12D and movie S10). Furthermore, the beat rate of Controls and cVOs both increased with the addition of isoproterenol, with cVO rates being consistently lower than Control

Science 5 JUNE 2025 8 of 22

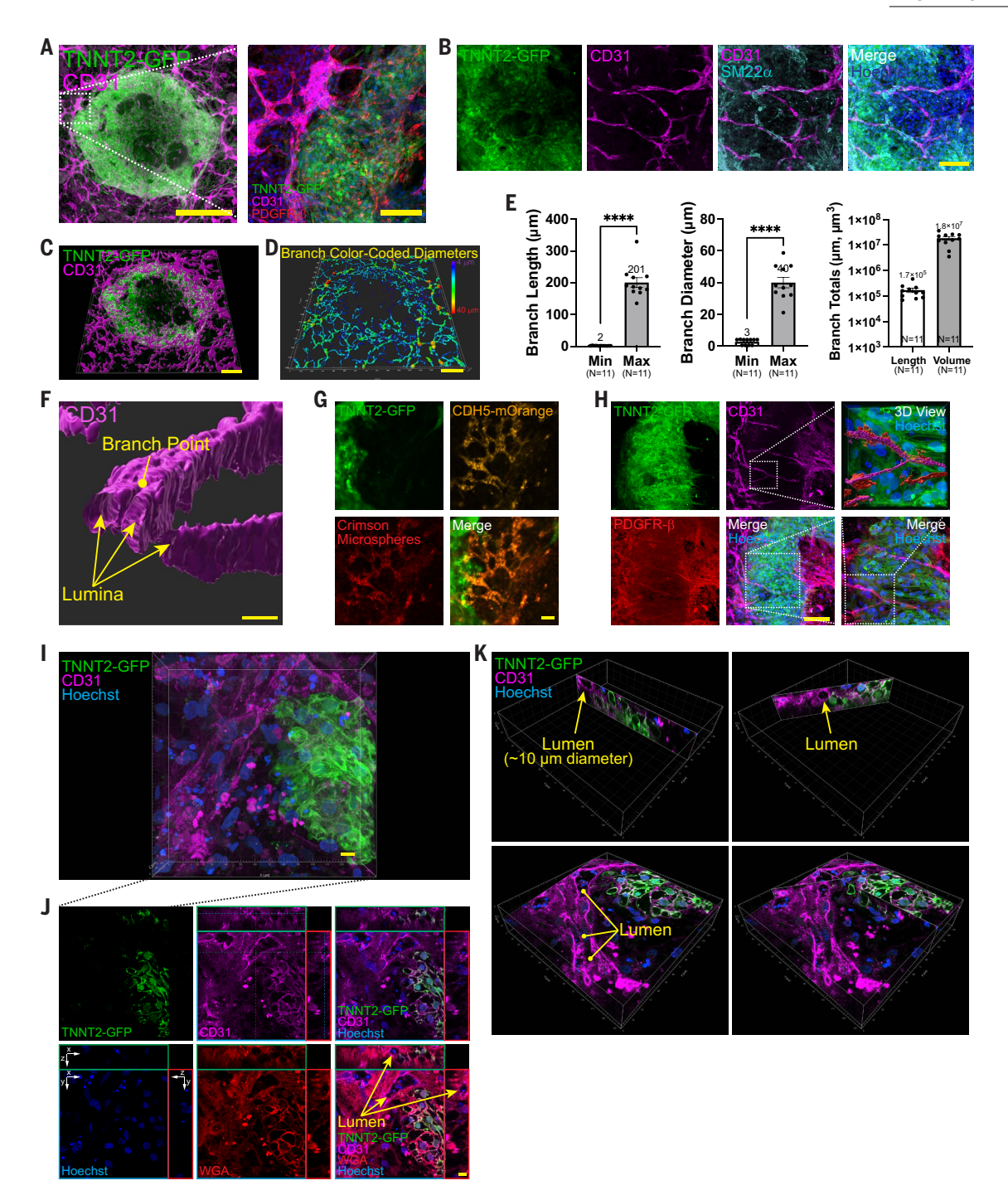


Fig. 5. cVOs comprise branched and lumenized vasculature spatially integrated with cardiomyocytes. (A) Maximum intensity projection (MIP) confocal images show a cVO (also shown in Fig. 4, A and B, and below in (C) and (D) with branched ECs (CD31, magenta) and PCs (PDGFR-β, red) integrated with and penetrating CMs (TNNT2-GFP, green). Scale bar, 0.5 mm (left), 100 μm (right). (B) MIP confocal images show SMCs (SM2 α , cyan) surrounding branched ECs (CD31, magenta) and integrated with CMs. Nuclei are labeled with Hoechst (blue). Scale bar, 100 μm. (C) 3D surface rendering shows ECs (CD31, magenta) integrated with CMs (TNNT2, green). Scale bar, 200 μm. (D) Three-dimensional surface rendering shows CD31 vascular branch color-coded diameters (4 to 40 μm). Scale bar, 200 μm. (E) Vascular branch length (min-max, 2 to 201 μm), diameter (min-max, 3 to 40 μm), and total length and volumes $(1.7 \times 10^5 \, \mu\text{m} \text{ and } 1.8 \times 10^7 \, \mu\text{m}^3)$ are consistent with a microvasculature phenotype. (F) Three-dimensional surface rendering shows ECs (CD31, magenta) forming three lumina and branches. Scale bar, 20 μm. (G) Confocal images show CMs (TNNT2-GFP, green), branched ECs (CDH5-mOrange, orange), and 1-μm-diameter microspheres (crimson) contained within EC branches. Scale bar, 50 μm. (H) MIP confocal images show PCs (PDGFR-β, red) surrounding branched ECs (CD31, magenta), within CMs (TNNT2-GFP, green). Nuclei are labeled with Hoechst (blue). Scale bar, 100 μm. (I) A high-magnification (63×) 3D MIP confocal image shows CMs (TNNT2-GFP, green) being integrated with ECs (CD31, magenta), which is also shown below in (J) and (K). Nuclei are labeled with Hoechst (blue). Scale bar, 10 μm. (J) Orthogonal cross-sectional confocal images (CD31, magenta), which is also shown below in (J) and (K). Nuclei are labeled with Hoechst (blue). Scale bar, 10 μm. (K) Nonorthogonal cross-sectional confocal images (oblique planes) of the 3D image in (I) shows lumen formation of ECs (CD31, magenta) around and within CM areas (TNNT2-GFP, green). Note

Science 5 JUNE 2025 9 of 22

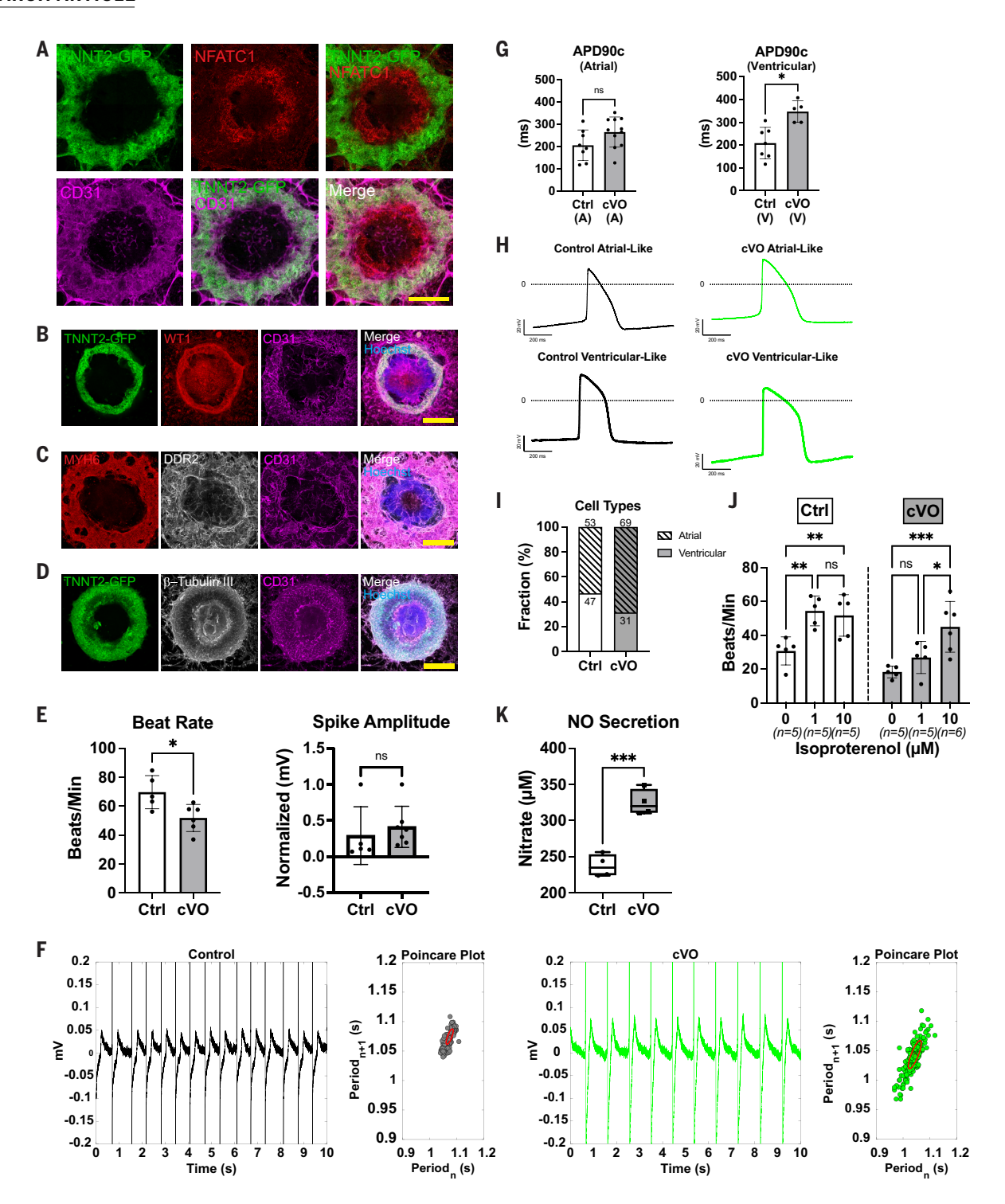


Fig. 6. cVOs comprise spatially integrated atrial, ventricular, endocardial, epicardial, and neuronal cell types. (A) MIP confocal images show an inner ring of endocardial cells (NFATC1, red) surrounded by an outer ring of CMs (TNNT2-GFP, green) and integrated with ECs (CD31, magenta). Scale bar, 0.5 mm. (B) MIP confocal images show epicardial cells (WT1, red) within the center of a cVO and in close proximity to CMs (TNNT2-GFP, green) and ECs (CD31, magenta). Nuclei are labeled with Hoechst (blue). Scale bar, 0.5 mm. (C) MIP confocal images show fibroblasts (DDR2, white) in close proximity to CMs (MYH6, red) and ECs (CD31, magenta). Nuclei are labeled with Hoechst (blue). Scale bar, 0.5 mm. (D) MIP confocal images show neuronal cells (β-Tubulin III, white) in close proximity to CMs (TNNT2-GFP, green) and ECs (CD31, magenta). Nuclei are labeled with Hoechst (blue). Scale bar, 0.5 mm. (E) MEA electrophysiology (EP) shows that cVOs beat significantly slower (*P < 0.05) than Controls without a significant difference in spike amplitude. ns, not significant. (F) MEA waveforms show cVOs with slower beating rates than Controls. Poincare plots are shown to the right. (G) Sharp electrode EP shows that corrected action potential duration at 90% repolarization (APD90c) is significantly higher (*P < 0.05) in cVO ventricular-like CMs compared with Control. (H) Sharp electrode waveforms show that cVO ventricular-like CMs have a longer action potential duration than Control ventricular-like CMs. (I) Analyzed cVOs comprise more atrial-like and less ventricular-like CMs compared with Control. (J) Beat rate of Controls (n = 15) and cVOs (n = 16) increases with isoproterenol (0, 1, and 10 μM) treatment, with Control rates consistently higher than cVO rates at each concentration. Two-way ANOVA with Tukey's test for multiple comparisons, *P < 0.05, **P < 0.005, ***P < 0.0005, ns, not significantly higher (****P < 0.0005) in cVO ECs compared with Control.

Science 5 JUNE 2025 10 of 22

rates at each concentration (Fig. 6J). However, compared to 3D approaches that use differentiated CMs combined with other cell types (15, 66, 68), contractility seems less developed and is a feature that warrants further enhancement, possibly through metabolic, electrical, and/or mechanical stimulation (69). Lastly, we observed that NO secretion was significantly higher in cVO ECs compared with Controls (***P < 0.0005) (Fig. 6K).

NOTCH and BMP pathway inhibition disrupts vasculature, whereas activation of the opioid pathway increases vasculature within cVOs

The NOTCH pathway is vitally important for cardiovascular development, disease, and regeneration (70). According to our bRNA-seq and scRNA-seq data, members of the NOTCH pathway, including JAG1, JAG2, DLL4, NOTCH1, NOTCH2, NOTCH3, and NOTCH4, were up-regulated in our cVOs (Fig. 4J, fig. S6C, and fig. S8F). Using scRNA-seq data from another cVO sample, we examined NOTCH-DLL-JAG receptor-ligand pairs between CMs, ECs, and SMCs to compare their putative cell-cell interactions in cVO and 6.5-PCW human heart groups (fig. S13A). The number of receptors and ligands, along with cell-cell interactions, were higher in the 6.5-PCW heart compared with the cVO, suggesting that NOTCH pathway activity is increased with increased vascularization and maturation.

To ascertain the effects of interfering with the NOTCH pathway on vascular and cardiac development, we next exposed cVOs to DAPT (N-[N-(3,5-difluorophenacetyl)-l-alanyl]-S-phenylglycine t-butyl ester), a known NOTCH pathway antagonist. From days 2 to 16, DAPT decreased EC formation in a dose-independent manner (1 μ M, n = 6, **P < 0.005; and 10 μ M, n = 6, **P < 0.005) compared with Control (n = 12) (fig. S13, B to D). DAPT also decreased CM formation at both 1 μ M (n = 6, **P < 0.005) and 10 μ M (n = 6, **P < 0.0005) compared with 0 μ M (Control) (n = 12) (Fig. S13, E to G). In addition, we fit a simple multiple linear regression model to the changes in EC and CM formation caused by DAPT (fig. S13, H and I). According to the temporal graphs (fig. S13, C, F, H, and I), the negative effect of DAPT on ECs was less than that on CMs.

According to our bRNA-seq and scRNA-seq data, the BMP pathway was up-regulated in cVOs. To ascertain the effects of interfering with the BMP pathway on vascular and cardiac development, we exposed cVOs to dorsomorphin, a known BMP pathway antagonist. Similar to the effect of DAPT, a dose-dependent inhibitory effect of dorsomorphin on EC formation was observed. From days 2 to 16, dorsomorphin decreased EC formation at 0.1 μ M (n = 6, ***P < 0.0005) and 1.0 μ M (n =6, ***P < 0.0005) compared with 0 μ M (Control) (n = 12) (fig. S14, A to C). Dorsomorphin at 1 μ M decreased CM formation (n = 6, **P < 0.005) compared with 0 μ M (Control) (n = 12), but 0.1 μ M dorsomorphin showed no significant inhibitory effects on CM formation (fig. S14, D to F). In parallel, we also fit a multiple linear regression model to the changes in EC and CM formation caused by dorsomorphin (fig. S14, G and H). According to the temporal graphs (fig. S14, B, E, G, and H), the negative effect of dorsomorphin on ECs was more pronounced than that on CMs; this was the opposite for DAPT. The codifferentiation of ECs and CMs in cVOs enabled this finding.

Next, we sought to use cVOs to reveal any teratogenic effects of fentanyl, a potent opioid agonist, which has contributed to the opioid epidemic in the United States in recent years (71) and may be misused during pregnancy, because up to 22% of women receive opioids during this period (72–74). However, the teratogenicity of opioids (75) remains uncertain, highlighting the need to use in vitro models to predict this risk for new and existing drugs, especially during the first few weeks of human pregnancy, which has been, until recently, a black box of development (76, 77). As fentanyl has been shown to activate multiple proangiogenic signaling pathways (78), we sought to observe any similar effects on cVO vascularization. At day 16, fentanyl, unlike DAPT or dorsomorphin, significantly increased EC formation at 10 nM (n = 18, **P < 0.005) compared with 0 nM (Control) (n = 18) (Fig. S14, I and J).

cVO vascularization factors also enable creation of hVOs

We next asked whether our cVO vascularization strategy could be applied to the hepatic system. On the basis of our micropatterning and transcriptomic results, we knew that we could produce mesoderm and endoderm, which is necessary for vascular and hepatic codifferentiation. Thus, our strategy for codifferentiation of ECs, SMCs, and HCs to create hVOs involved inducing mesendoderm and then codifferentiating vascular progenitor and hepatoblast pools to produce all three cell types (Fig. 7A). The timeline, cell types, geometry, media, and growth factors for creating hVOs are shown in fig. S15A. We used previously established methods to guide mesendoderm, foregut progenitor, hepatoblast, and immature hepatocyte formation (4, 79) (fig. S15B).

We tested three differentiation conditions as follows: (i) hVO-Control (day 20 baseline hepatic differentiation, with no vascularization factors added), (ii) hVO-D3 (day 20 hVOs created by adding vascularization factors at day 3 of differentiation and onward), and (iii) hVO-D6 (day 20 hVOs created by adding vascularization factors at day 6 of differentiation and onward) (table S5). We used the hESC-3R line, which enables vascular formation to be sequentially visualized, and then performed endpoint immunostaining for hepatic, cholangiocyte, and vascular markers. Under our hepatic differentiation conditions, we did not observe any GFP fluorescence, which indicated no production of "contaminating" CMs.

WGCNA showed clustering of pluripotency genes, structural genes, miscellaneous hepatic genes, hepatic and nonhepatic endoderm genes, hepatic and smooth muscle cell genes, and vascularization genes. Vascularization genes were the most up-regulated in the hVO-D3 group (Fig. 7B). PCA of temporal bRNA-seq showed developmental differences among hESC-3R (day 0 undifferentiated micropatterns), hVO-Control, hVO-D3, and hVO-D6 groups (n=3 for each group). There was a notable divergence between the "Vascularization Factors" (D3 and D6) versus "No Vascularization Factors" (hVO-Control) groups (fig. S15C).

Notably, our bRNA-seq results showed that the expression of hepatic (SERPINAI and HGF), cholangiocyte (HNFIB), endothelial cell (CDH5), and smooth muscle cell (TAGLN) genes were the most up-regulated for the hVO-D3 group, with CDH5 and TAGLN higher than in the other groups (Fig. 7C). Furthermore, bRNA-seq showed expression of pluripotency, HC/cholangiocyte, EC, NOTCH-DELTA-JAG, SMC/PC, FB/ECM, and hematopoietic genes across all four groups, with the hVO-D3 group having the highest vascular gene expression while expressing markers of immature HCs, cholangiocytes, FBs, and hematopoietic cell types (fig. S15D). This is consistent with our previous work showing that hepatic organoid cultures pass through stages that resemble those occurring during embryonic development, with many of the cells in day 20 organoid cultures remaining immature and resembling those of fetal liver (4, 80).

From days 3 to 19, time-lapse fluorescence microscopy showed EC formation for all three groups (n=10,12, and 10, respectively). Adding vascular factors at day 3 (hVO-D3 group) to the baseline hepatic differentiation protocol produced the highest EC formation at day 19 (**P<0.005, ***P<0.0005) (Fig. 7, D to F). Confocal fluorescence imaging demonstrated the codifferentiation of immature HCs (AFP⁺) and ECs (CDH5-mOrange⁺) at day 19 of differentiation (Fig. 7G).

As with our cVOs, to further characterize hVO we used MIP confocal imaging and Imaris software –enabled 3D surface rendering of various cell type –specific markers. hVOs included vasculature with ECs (CDH5⁺, LYVE⁺, and THBD⁺) integrated with centrally located SMCs (TAGLN-CFP⁺ and SMA⁺) (Fig. 7H) and with THBD and LYVE markers colocalizing with CD31⁺/CDH5-mOrange⁺ ECs (Fig. 7I and fig. S15E), which is consistent with a liver sinusoidal endothelial cell (LSEC) phenotype. Dispersed with immature AFP⁺ HCs were CK19⁺ cholangiocytes surrounding centrally located TAGLN-CFP⁺ SMCs (Fig. 7J).

hVOs also comprised ALB⁺ HCs that coexpressed AFP, interspersed with THBD⁺ LSECs (fig. S15F). As expected for a differentiation duration of only 20 days, albumin production of all four groups was low at about one-third of primary human hepatocytes (PHH), without appreciable difference between groups (fig. S15G).

Science 5 JUNE 2025 11 of 22

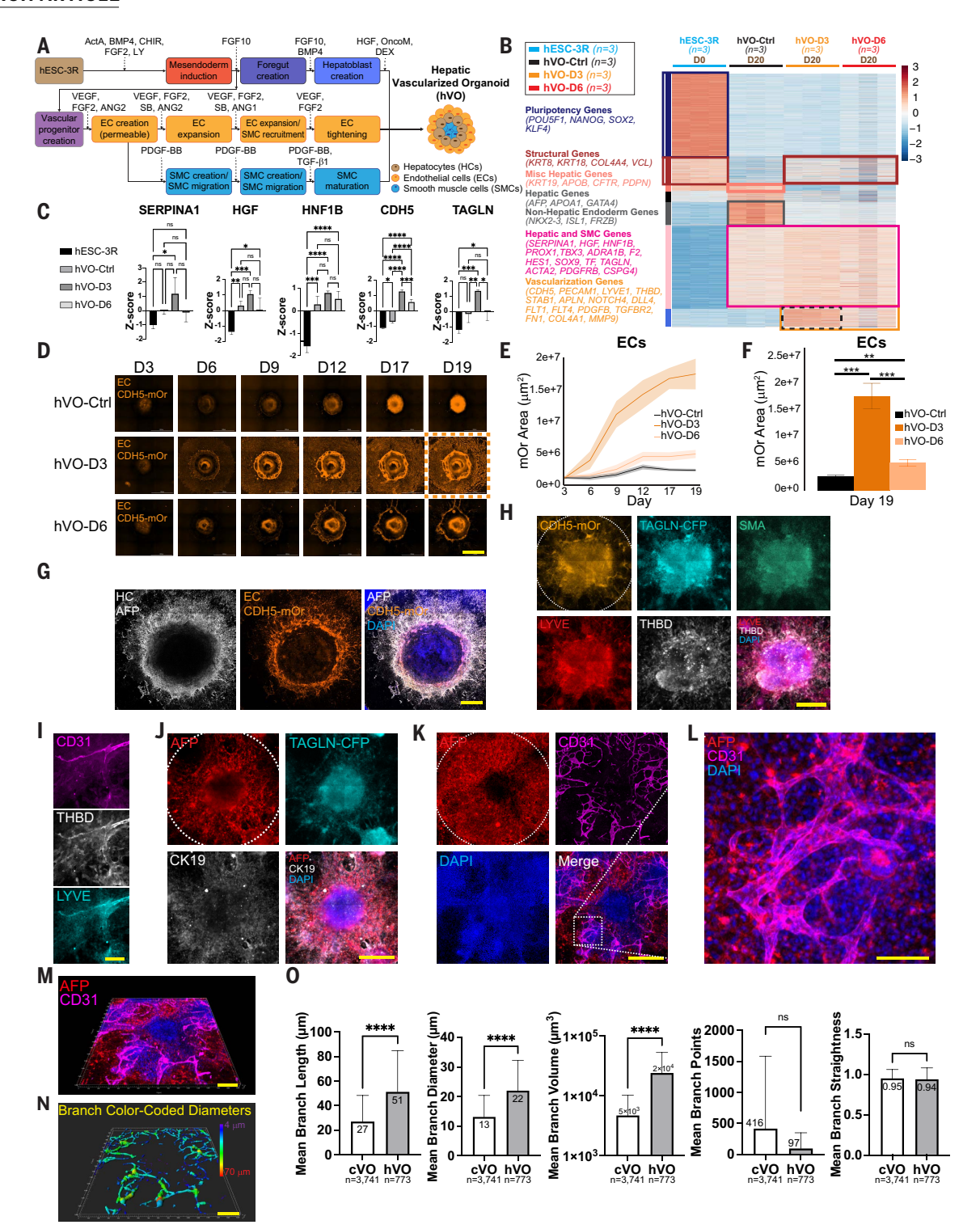


Fig. 7. Vascularization factors used for creating cVOs enable creation of hVOs. (**A**) Strategy for codifferentiating HCs (immature), ECs, and SMCs to create hVOs. Key steps are inducing mesendoderm and then codifferentiating hepatoblasts and vascular progenitors into all three cell types. HC, hepatic cells. (**B**) Bulk RNA-seq WGCNA heatmap showing clusters of pluripotency, structural, miscellaneous hepatic, hepatic and nonhepatic endoderm, hepatic and smooth muscle cell, and vascularization genes for day 0 (D0) hESC-3R (blue, n = 3), and differentiation over 20 days (D20) for Control (black, n = 3), hVO-D3 (orange, n = 3), and hVO-D6 (red, n = 3) groups. Black dashed rectangle shows vascularization genes are most up-regulated in the hVO-D3 group. (**C**) Comparison between hESC-3R, hVO-Control, hVO-D3, and hVO-D6 for hepatocyte (*SERPINA1*, *HGF*), cholangiocyte (*HNF1B*), endothelial cell (*CDH5*), and smooth muscle cell (*TAGLN*) gene expression. Notably, all genes are most up-regulated for the hVO-D3 group, with *CDH5* and *TAGLN* significantly higher. One-way analysis of variance (ANOVA) with Tukey's test for multiple comparisons, *P < 0.05, **P < 0.005, ***P < 0.0005, ****P < 0.

Science 5 JUNE 2025 12 of 22

(left), ECs (CDH5-mOrange, orange) (middle), and merge (right). Note the endoderm-derived immature HC ring concentrically surrounding the mesoderm-derived EC ring. Nuclei are labeled with DAPI (blue). Scale bar, 0.5 mm. (\mathbf{H}) MIP confocal images show an hVO with ECs [CDH5-mOr, orange; LYVE (lymphatic vessel endothelial hyaluronan receptor), red; THBD (thrombomodulin), white] integrated with centrally located SMCs (TAGLN-CFP, cyan; SMA, green). Nuclei are labeled with DAPI (blue). Dotted white circle outlines the hVO. Scale bar, 0.5 mm. (\mathbf{I}) MIP confocal images show that ECs coexpress CD31 (magenta), THBD (white), and LYVE (cyan) within an hVO. Scale bar, 200 μ m. (\mathbf{J}) MIP confocal images show an hVO with immature HCs (AFP, red) and cholangiocytes (CK19, white) surrounding centrally located SMCs (TAGLN-CFP, cyan). Nuclei are labeled with DAPI (blue). Dotted white circle outlines the hVO. Scale bar, 0.5 mm. (\mathbf{K}) MIP confocal images show an hVO with immature HCs (AFP, red) integrated with ECs (CD31, magenta) [also shown below in (\mathbf{M}) to (\mathbf{N})]. Nuclei are labeled with DAPI (blue). Dotted white circle outlines the hVO. Scale bar, 0.5 mm. (\mathbf{L}) Enlarged square region of (\mathbf{K}). Scale bar, 100 μ m. (\mathbf{M}) Three-dimensional surface rendering shows ECs (CD31, magenta) integrated with immature HCs (AFP, red). Scale bar, 200 μ m. (\mathbf{N}) Three-dimensional surface rendering shows CD31 vascular branch color-coded diameters (4 to 70 μ m). Scale bar, 200 μ m. (\mathbf{O}) hVO branch length (51 versus 27 μ m), mean branch diameter (22 versus 13 μ m), and mean branch volume (2 × 10⁴ versus 5 × 10³ μ m³) are significantly higher than cVO. hVO mean branch points (97 versus 416) and mean branch straightness (0.94 versus 0.95) are not significantly different compared with cVO counterparts. Student's t test, ****P < 0.00005, ns, not significantly different compared with cVO branches and 773 hVO branches).

hVOs comprised CD31⁺ EC/LSEC branches that integrated with AFP⁺ immature HCs (Fig. 7, K and L). Imaris 3D surface rendering of the same hVOs shows a network of ECs integrated with the AFP⁺ immature HCs (Fig. 7M), with ECs forming vascular branches with diameters ranging from 4 to 70 μm (Fig. 7N), larger on average than those of cVOs. Quantification confirmed that hVO vasculature had a significantly larger mean branch length, diameter, and volume than cVO vasculature (all *****P < 0.00005) (Fig. 7O).

Additionally, hVOs contained CD31 $^+$ ECs surrounded by LGR5 $^+$ adult stem cells, Muc2 $^+$ intestinal-related cells, and ChgA $^+$ neuroendocrine cells, suggesting that the hVO differentiation protocol also gives rise to other endoderm derivatives (fig. S15, H to J).

To examine hepatogenic and vascularization potential of hVOs created from hiPSCs, we differentiated hVOs from five randomized hiPSC lines (table S6). hVOs had significantly more ECs (**P < 0.005, ****P < 0.0005, ****P < 0.00005) compared with Controls for each line while maintaining various amounts of HCs (fig. S16, A to C). As with cVOs, the quantity of ECs varied among different hiPSC lines.

Discussion

Using clues from developmental biology, we created spatially self-organized cVOs by identifying a combination of growth factors that simultaneously gave rise to a spatially organized and branched vascular network within endocardial, myocardial, epicardial, and neuronal cells. Using scRNA-seq and imaging, we showed a similar overall cellular composition of cVOs to a 6.5-PCW human heart, with cVOs containing fewer hematopoietic cell types. Other investigators have very recently described methods to codifferentiate hematopoietic cells within cardiac and hepatic organoids (35, 81), which could be integrated with our current cVO differentiation protocol upon further optimization.

Although our manual stencil-based micropatterning method limits throughput, commercially available coverslips with preprinted ECM micropatterns (46), microcontact printing (82), and 3D bioprinting (21) are alternatives, some of which are amenable to automation. In micropatterns, a wave of WNT signaling balanced by secreted inhibitors and activators controls primitive streak formation (48), and mechanical tension contributes to mesoderm specification (83, 84).

Several recent studies have demonstrated the creation of 3D cardiac organoids (28–33) with ECs and ENDOs lining central chambers. However, complex vascular branching was rarely detected, and the increase in EC/ENDO density has been mostly achieved by the addition of VEGF (14). In our screening conditions, we added additional growth factors and a small molecule to systematically promote vasculogenesis, followed by angiogenesis, vessel branching, and lumen formation. Furthermore, our hESC-3R line enabled temporal tracking of this developmental process, with micropatterning identifying spatial relationships. FGF2 (85), combined with VEGF and SB has been shown to produce vascular organoids (17, 24). VEGF promotes vasculogenesis, whereas the addition of FGF2 with VEGF promotes angiogenesis (55), and the addition of SB to these two factors increased hPSC-EC differentiation by up to 36-fold (6). Additionally, ANG2 also promotes angiogenesis, and the subsequent addition of ANG1 promotes

vessel maturation (54, 55, 58); we found that several angiopoietinrelated genes were up-regulated in cVOs. Lastly, the addition of PDGF-BB recruits mural cells (PCs and SMCs) to wrap around angiogenic sprouts, and the addition of TGF- β 1 leads to vessel maturation by inhibiting EC proliferation, stimulating SMC differentiation, and promoting ECM deposition (54, 55). In support of this, we found that several members of the PDGF and TGF β gene expression pathways were up-regulated, and immunostaining validated the presence of SMCs and PCs in our cVOs, which correlated with increased vascularization. Furthermore, we showed that SMCs and PCs wrapped around ECs to form branched and lumenized vasculature intimately integrated with CMs.

Our temporal bulk and endpoint single-cell transcriptomics revealed several important cell types and pathways for cardiogenesis and vasculogenesis (86), including the NOTCH and BMP pathways. Our interference with relatively selective inhibitors of these pathways (DAPT and dorsomorphin) confirmed their general disruptive effects on vascularization. By investigating the interaction between cardiac and vascular cell types, our system could be used to further dissect the role of NOTCH in hypoplastic left heart syndrome (87), the TGF β pathway in left ventricular noncompaction (88), and the PDGF pathway in lamin A/C cardiomyopathy (89). These pathways were all up-regulated in our cVOs, highlighting their important roles in cardiogenesis and vascularization.

Lastly, using the same combination of vascular-inducing factors to create cVOs and hVOs implies a conserved developmental program is involved in creating vasculature in different organ systems. Leveraging the RUES-GLR germ layer reporter line, various progenitor reporter lines, and parenchymal cell-specific reporter lines, our vascularization method serves as a starting point that can facilitate the development of cell-specific differentiation protocols to achieve vascularization in other organ systems.

Materials and methods

All experiments, methods, and protocols for this study were approved by the Stanford University Stem Cell Research Oversight (SCRO) committee. Key materials, reagents, software, and equipment are listed in table S7 and will be provided upon reasonable request.

Human pluripotent stem cell (hPSC) lines

We used the following hPSC lines (both hESC and hiPSC). The H9 WT hESC (WA09, WiCell) was previously used as the parental line to create the H9 hESC-NKX2-5-eGFP line (51) and the H9 hESC-TNNT2-GFP line (H9-hTnnT2-pGZ-TD2, WiCell) (52). In our study, we used the hESC-TNNT2-GFP line to create the hESC-triple reporter (3R) line (described in more detail in the Reporter Cell Line Creation section below). To fluorescently visualize mesoderm, endoderm, and ectoderm germ layers, we used the hESC-RUES-GLR line generously provided by the Brivanlou Lab (49). Initially, we used the 113 WT hiPSC line (Stanford CVI Biobank) to validate our hESC cVO results. We subsequently used the additional hiPSC lines (Stanford CVI Biobank) listed in tables S4 and S6 to further validate cVO and hVO creation.

Science 5 JUNE 2025 13 of 22

Relevant biological variables

The hESC-3R and hESC-RUES-GLR lines were derived from female donors (race/ethnicity unknown) while the 113 hiPSC line was derived from a White (not Hispanic) male donor. The additional hiPSC lines used to further validate cVO and hVO creation were derived from donors of various sexes and races/ethnicities listed in tables S4 and S6.

Construction of lentiviral plasmids

The two final lentiviral vector plasmids pLV-CDH5Pr-mOrange-SVPr-Zeo and pLV- TAGLNPr-CFP-SVPr-Bsd were constructed as described below. To facilitate selection and identification of cell lines transduced with lentivirus created with these vectors, we designed a series of double-cassette lentiviral vectors that feature cell-specific fluorescent reporter cassettes and constitutively expressed drug-selection cassettes. The overall design of these vectors is illustrated in fig. S2, E to H.

First, a blank lentivirus vector pLV-B was derived from pSicoR (11579, Addgene). The plasmid pSicoR was digested by ApaI-EcoRI, and religated with an oligo adaptor (Adaptor-A/B) containing restriction sites XhoI, NotI, XbaI, and XmaI. The oligo adaptor and PCR primers used in this study are listed in table S8.

Next, a cassette with the SV40 promoter (SVPr) controlling the expression of Zeocin (Zeo) was introduced into the blank lentivirus vector pLV-B to create the plasmid pLV-SVPr-Zeo. The template for the SVPr comes from the pGL3 luciferase reporter plasmid (E1741, Promega), and Zeo from the pGreenZeo human Nanog reporter plasmid (SR10030VA-1, System Biosciences). The cassette SVPr-Zeo was assembled by PCR with primer pairs SVPr-F/R and Zeo-F/R as previously described (90). The derived fragment was restricted with XbaI-XmaI and ligated into pLV-B at the same sites to create pLV-SVPr-Zeo.

Then, the Blasticidin (Bsd) coding sequence (CDS) was introduced to replace the Zeocin CDS in pLV-SVPr-Zeo. The Bsd CDS was amplified from the pCMV/Bsd (BsdCassette Vector) plasmid (V51020, Thermo Fisher) with primer pair Bsd-F/R. The amplified fragment was digested with AgeI-XmaI and ligated into pLV-SVPr-Zeo at the same sites. Thus, the plasmid pLV-SVPr-Bsd was created.

The plasmid pLV-CDH5Pr-mOrange-SVPr-Zeo was constructed as follows. The cassette carrying the CDH5 (VE-cadherin) promoter (CDH5Pr) controlling expression of the mOrange fluorescent protein was amplified from the plasmid pLV-CDH5Pr-mOrange (91), which is a gift from Dr. Shahin Rafii (Weill Cornell Medicine), with primer pair VmO-F/R. The amplified fragment was restricted with XhoI-XbaI and ligated into pLV-SVPr-Zeo at the same sites to create pLV-CDH5Pr-mOrange-SVPr-Zeo.

The plasmid pLV-TAGLNPr-CFP-SVPr-Bsd was constructed by inserting a human transgelin (TAGLN) (SM22-alpha) promoter-directed CFP cassette (TAGLNPr-CFP) into pLV- SVPr-Bsd. This TAGLNPr-CFP cassette was obtained by PCR assembly of the TAGLNPr and the CFP CDS with primer pairs TGN-F/R and CFP-F/R as previously described (90). The TAGLN promoter sequence comes from the pEZX-TAGLN-GLuc plasmid (HPRM24364- PG02GeneCopoeia), and the CFP CDS from the pTagCFP-N plasmid (FP112, Evrogen). The derived fragment was restricted with XhoI-XbaI and ligated into pLV-SVPr-Bsd at the same sites to create pLV-TAGLNPr-CFP-SVPr-Bsd. Verification of plasmid construction was done by Sanger sequencing.

Lentivirus production

To package plasmid in lentivirus, HEK 293FT cells (R70007, Thermo Fisher) were transfected separately with target plasmids [pLV-CDH5Pr-mOrange-SVPr-Zeo or pLV- TAGLNPr-CFP-SVPr-Bsd, and the packaging plasmids psPAX2 (containing GAG and POL) (12260, Addgene) and pMD2.G (containing VSV-G) (12259, Addgene)] using Lipofectamine 2000 (11668019, Thermo Fisher). Transfected HEK293FT cells were incubated for 3 days and media collected daily. Media was then centrifuged at 3000 g for 15 min to remove cells and cell debris. The supernatant was concentrated using PEG-it Virus Precipitation Solution (LV810A, System Biosciences) according to the manufacturer's protocol.

Reporter cell-line creation

The H9 hESC-TNNT2-GFP cell line (52) (H9-hTnnT2-pGZ-TD2, WiCell) was seeded on 6-well plates and first transduced with the lentivirus expressing CDH5Pr-mOrange-SVPr-Zeo. Cells were selected by Zeocin (0.5 to $3 \,\mu g/ml$) treatment for 1 to 2 weeks. Genomic DNA was isolated from several clones, PCR was performed, and gel electrophoresis was used to verify expression of CDH5 (VE-cadherin), mOrange, and Zeocin. This double reporter cell line was then transduced with the lentivirus expressing TAGLNPr-CFP-SVPr-Bsd to create the H9 hESC-triple reporter (3R) cell line (hESC-3R). Cells were selected by Blasticidin ($3 \,\mu g/ml$) treatment for 1 to 2 weeks. Again, genomic DNA was isolated from several clones, PCR was performed, and gel electrophoresis was used to verify the presence of TAGLN (SM22-alpha), CFP, and Blasticidin (fig. S2, I to K). PCR primers are listed in table S8.

Nonquantitative PCR

Nonquantitative PCR was performed using custom-designed PCR primers (table S8). Genomic DNA was isolated with the PureLink Genomic DNA Mini Kit (K182000, Thermo Fisher) and quantified using a Nanodrop 2000 Spectrophotometer (ND-2000, Thermo Fisher) per the manufacturer's instructions. For PCR amplification, AccuPrime SuperMix I (12342, Thermo Fisher), custom primers for pluripotency and lentiviral markers (table S8), and genomic DNA were combined. Non-template control (NT) reactions were prepared by substituting DNA with distilled water. Samples were transferred to a thermal cycler and the following cycling program was used: (i) initial denaturation at 94°C for 2 min; (ii) 30 cycles of 94°C, 30 s; 60°C, 30 s; 68°C, 1 min; and (iii) final extension at 68°C for 5 min. Reactions were maintained at 4°C after cycling and then stored at -20°C. The PCR products and a 10- to 1500-bp DNA QuantLadder (50475, Lonza) were loaded in a 1.2% 16+1 double-tier FlashGel DNA Cassette (57029, Lonza), run, and visualized with the FlashGel System (57067, Lonza).

hPSC culture

The hPSC lines (both hESCs and hiPSCs) were maintained in the pluripotent state through daily feeding with Essential 8 (E8) medium and supplement (A1517001, Thermo Fisher Scientific). The medium was changed daily, and cells were passaged every 3 to 4 days with 0.5 mM EDTA (15575-020, Thermo Fisher Scientific) between a 1:6 and 1:12 split ratio. hPSCs were passaged onto tissue culture plates coated with Corning Matrigel membrane matrix (354234, Thermo Fisher Scientific) at a dilution of 1:100 for either maintenance or differentiation. To aid in passaging undifferentiated hPSCs by minimizing anoikis (dissociation-induced apoptosis), we cultured cells for 24 hours with 10 μ M ROCK inhibitor Y-27632 (HY-10583, MedChem Express). Excess cells were frozen in 90% Knockout Serum Replacement (KOSR) (#10828010, Thermo Fisher Scientific) with 10% DMSO (#D2438, Sigma-Aldrich) in cryovials and frozen at -80° C overnight and then subsequently transferred to liquid nitrogen storage.

Pluripotency markers

Using standard protocols, undifferentiated hPSCs were labeled with primary antibodies for the pluripotency markers Oct-3/4 (mouse antihuman Oct-3/4 mAb (Clone 40), 1:400, 611202, BD Biosciences), Nanog (goat anti-human Nanog pAb, 1:100, AF1997, R&D Systems), and Sox2 (rabbit anti-human Sox2 mAb (Clone D6D9), 1:200, 3579S, Cell Signaling Technology). Secondary antibodies used were donkey anti-mouse IgG Alexa 488 for Oct-3/4, 1:500 (A21202, Thermo Fisher Scientific); donkey anti-goat IgG Alexa 555 for Nanog, 1:500 (A21432, Thermo Fisher Scientific); and donkey anti-rabbit IgG Alexa 647 for Sox2, 1:500 (A31573, Thermo Fisher Scientific). Cell nuclei were counterstained with 4′,6-diamidino-2-phenylindole (DAPI) (#D8417, Sigma-Aldrich, 1 mg/ml + 0.1% Triton X-100 in PBS) or DRAQ5 Fluorescent Probe Solution (5 mM) (62251, Thermo Fisher Scientific). Primary and secondary antibodies are listed in table S7.

Science 5 JUNE 2025 14 of 22

Stencil creation for hPSC colony micropatterning

Our previous micropatterning method (25) used a high-cost laser cutter that is not available in many labs. Here, to create stencils for hPSC colony micropatterning, we used a low-cost, widely available, table-top Silhouette Cameo cutting tool (B007R83VKE, Silhouette America, Amazon) to design and then cut circular patterns from a silicone sheet (P18178, Thermo Fisher Scientific, or 785GL6, Grainger, or HT-6220, Rogers Corporation). To fit in one well of a standard Falcon 48-well plate (353078, Thermo Fisher Scientific), the outer diameter of the circular patterns was cut to approximately 9.5 mm. To fit in one well of a standard Falcon 6-well plate (353046, Thermo Fisher Scientific), the outer diameter of the circular patterns was cut to approximately 34 mm. At the center of the 48-well pattern, a single 2-mm hole was cut to create a complete single-hole stencil; for the 6-well circular pattern, an evenly spaced array (3 by 3 to 7 by 7 with a pitch of 2 to 5 mm from center to center) of 2-mm holes were cut to create a complete multi-hole stencil array. The stencils were then washed three times with deionized (DI) water for 20 min. For previously used stencils, cleaning was performed three times for 30 min with Alconox anionic detergent (ALC1104, Midland Scientific) in an ultrasonic cleaning bath (Branson Ultrasonic Bath, Emerson Electric) to remove any residual cellular debris. After detergent cleaning, stencils were washed again six times with DI water for 15 min in the ultrasonic bath. Next, to render the silicone stencil surfaces hydrophilic, a handheld laboratory corona treater (12051A, Electro-Technic Products) was swept back and forth across the stencils approximately four to six times for 30 sec. The stencils were then autoclaved at 15 psi at 121°C for 30 min. Finally, the stencils were kept submerged in 100% ethanol until they were ready to be placed in the multi-well plates.

Single and multiple hPSC colony micropatterning

Stencils for either a 48-well plate or a 6-well plate were placed in each well and pressed onto the well surface with sterile forceps. Next, ice cold Corning Matrigel membrane matrix (354234, Thermo Fisher Scientific) at a dilution of 1:100 in 0.25 ml ice cold RPMI-1640 (11875-093, Thermo Fisher Scientific) was poured into each well containing a stencil and was gelled by incubating at 37°C for at least 1 hour. Undifferentiated hPSCs were dissociated with 0.5 mM EDTA (15575-020 Gibco/ Thermo Fisher Scientific) and passaged as a single cell suspension that included 10 µM of the Y-27632 (HY-10583, MedChem Express) to prevent dissociation-induced apoptosis. The cells at a concentration of $1.0 - 1.5 \times 10^6$ cells/ml were introduced into the Matrigel- and stencilcontaining wells and were allowed to attach at 37°C overnight in 0.25 ml Essential 8 (E8) medium. The next day, stencils were removed with sterile forceps, leaving micropatterned cells attached on the 2-mm circular islands created by the 2-mm holes of the stencils. At this concentration, the 2-mm colonies were essentially 100% confluent in 2 to 3 days, showing good border integrity and uniform cell density. When colonies were filled in, the cells were fed with ice cold E8 which contained Matrigel at a dilution of 1:100 and immediately placed back in the incubator to minimize cold shock. This was required to allow the colonies to migrate beyond their 2-mm initial boundaries upon differentiation. The differentiation protocol was initiated when the colonies were essentially 100% confluent, typically 2 to 3 days after seeding. We observed successful differentiation on circular micropatterns at diameters of 2, 4, and 6 mm, but chose 2 mm because this size gave more repeatable results and allowed greater outward migration within the 48-well plates.

Growth factors and small molecules

To induce mesoderm and subsequent cardiomyocyte differentiation, we used 4, 5, or 6 μM CHIR (S2924, Selleck Chemicals) and 5 μM IWR (S7086, Selleck Chemicals) and 5 ng/ml FGF2 (100-18B, PeproTech). These two small molecules and one growth factor served as the basis for our baseline (Control group) differentiation method (described in more detail in the Baseline Cardiomyocyte Differentiation section).

To simultaneously induce endothelial cell vasculogenesis and angiogenesis along with cardiomyocyte differentiation (described in more detail in the Cardiovascular Differentiation section), we added 50 ng/ml VEGF (100-20, PeproTech); 5 ng/ml FGF2 (100-18B, PeproTech); 10 μ M SB (S1067, Selleck Chemicals); 50 ng/ml ANG2 (130-07, PeproTech); 50 ng/ml ANG1 (130-06, PeproTech); and select components of the VascuLife VEGF LifeFactors Kit (LS-1020, Lifeline Cell Technology) [5 ng/ml EGF, 15 ng/ml IGF-1, 50 μ g/ml ascorbic acid, 0.75 U/ml heparin sulfate, 1 μ g/ml hydrocortisone, 5 ng/ml VEGF (not added), 5 ng/ml FGF2 (not added), 2% FBS (not added), 30 mg/ml/15 μ g/ml gentamicin/amphotericin B (not added), and 10 mM glutamine (not added)].

To simultaneously induce smooth muscle cell differentiation with cardiomyocyte and endothelial cell differentiation (described in more detail in the Cardiovascular Differentiation section), we added 2.5 or 10 ng/ml PDGF-BB (100-14B, PeproTech) and 0.5 or 2 ng/ml TGF- β 1 (100-21C, PeproTech).

Finally, to maintain isolated ECs, we used the EGM-2 Bullet Kit (CC-3162, Lonza) [EGF, IGF-1, ascorbic acid, heparin sulfate, hydrocortisone, VEGF, FGF2, FBS, and gentamicin/amphotericin-B (manufacturer does not provide concentrations)].

To induce mesendoderm and subsequent hepatocyte differentiation (described in more detail in the Hepatovascular Differentiation section), we used 100 ng/ml Activin-A (338-AC, R & D Systems); 10 ng/ml BMP-4 (314-BP, R & D Systems); 3 μ M CHIR (S2924, Selleck Chemicals); 10 μ M LY294002 (PI3K-AKT inhibitor) (70920, Cayman Chemical Company); 50 ng/ml FGF-10 (100-26, PeproTech); 50 ng/ml HGF (100-39H, PeproTech); 50 ng/ml Oncostatin-M (300-10, PeproTech); 10 μ M Dexamethasone (1126/100, Tocris); and HCM Hepatocyte Culture Medium Bullet Kit (CC-3198, Lonza).

Baseline CM differentiation

For baseline CM differentiation (Control group), hPSCs were transferred to Matrigel-coated non-micropatterned and micropatterned surfaces as described above and differentiated in RPMI-1640 media (61870036, Thermo Fisher Scientific) supplemented with B27 without insulin (A1895601, Thermo Fisher Scientific). Our baseline differentiation method was based on a previously described small molecule-based monolayer method (3, 92). Briefly, on the first day (day 0) of differentiation, basal medium was supplemented with 4, 5, or 6 µM CHIR (S2924, Selleck Chemicals) and 5 ng/ml FGF2 (100-18B, PeproTech). On day 2, the medium was replaced with basal medium containing B27 without insulin. On day 3, the medium was replaced with basal medium containing B27 without insulin and containing 5 μM IWR (S7086, Selleck Chemicals). On day 5, the medium was replaced with basal medium containing B27 without insulin. From days 7 to 16, the basal medium was changed to contain B27 with insulin (17504044, Thermo Fisher Scientific) and was replaced every 48 hours thereafter. CMs generally began spontaneously beating sometime between days 7 and 10. hPSC-CMs were collected on day 16 for further downstream studies. More complex cardiac vascularized organoid (cVO) differentiation described below was based on this baseline differentiation and contained several additional small molecules and growth factors to promote simultaneous cardiac and vascular codifferentiation.

EC differentiation

We differentiated ECs from hPSCs as previously described (53). Briefly, hPSCs were seeded on Matrigel-coated plates in E8 medium (A1517001, Thermo Fisher Scientific) to 50% confluency. At 80% confluency, hPSCs were differentiated toward the mesodermal lineage by treatment of 6 μ M CHIR (S2924, Selleck Chemicals) in RPMI-1640 media (61870036, Thermo Fisher Scientific) supplemented with B27 without insulin (A1895601, Thermo Fisher Scientific) for 2 days, followed by a second treatment of 2 μ M CHIR in RPMI-B27 without insulin for 2 days. At day 4 of differentiation, the cells were subjected to a differentiation medium comprised of RPMI-B27 without insulin

Science 5 JUNE 2025 15 of 22

and the EGM-2 Bullet Kit (CC-3162, Lonza) supplemented with 20 ng/ml BMP-4 (314-BP, R & D Systems), 50 ng/ml VEGF (100-20, PeproTech), and 20 ng/ml FGF2 (100-18B, PeproTech). Cells were subjected to medium change every 2 days, where the concentration of RPMI-B27 without insulin was gradually decreased and replaced by EGM-2 by day 10. On day 12, the differentiating hPSC-ECs were isolated using magnetic-activated cell sorting (MACS), where cells were dispersed by TrypLE (12563011, Thermo Fisher Scientific), incubated with bead-conjugated anti-VE-cadherin antibody (130-097-857, Miltenyi Biotec), and sorted with a MiniMACS separator (130-090-312, Miltenyi Biotec). Sorted VE-cadherin+ cells were collected and seeded on 0.2% gelatin (G1393, Sigma-Aldrich)-coated plates and maintained in EGM-2 medium supplemented with 10 μ M SB (S1067, Selleck Chemicals), a TGF- β 1 inhibitor.

Smooth muscle cell (SMC) differentiation

We prepared basal, induction, and maintenance media and differentiated SMCs as previously described (8). Briefly, basal chemically defined medium (CDM) consisted of 50% vol/vol IMDM (12440053, Thermo Fisher Scientific), 50% vol/vol Ham's F-12 Nutrient Mix (11765054, Thermo Fisher Scientific), 1% vol/vol chemically defined lipid concentrate (11905031, Thermo Fisher Scientific); 2 mM Glutamax supplement (35050061, Thermo Fisher Scientific), 1 mg/ml Poly(vinyl) alcohol (PVA) (P8136, Sigma-Aldrich), 7 μg/ml insulin (I9278, Sigma-Aldrich), $15\,\mu g/ml$ transferrin (11107018, Thermo Fisher Scientific), and $450\,\mu M$ 1-thioglycerol (M6145, Sigma-Aldrich). Neural crest (NC) induction medium consisted of CDM, 1 µM CHIR (S2924, Selleck Chemicals), 2 μM SB (S1067, Selleck Chemicals), 250 nM LDN193189 (S2618, Selleck Chemicals), and 15 ng/ml BMP-4 (314-BP, R & D Systems). Neural crest (NC) maintenance medium consisted of CDM, 10 ng/ml FGF2 (100-18B, PeproTech), 10 ng/ml EGF (AF-100-15, PeproTech), and 2 μM SB (S1067, Selleck Chemicals). SMC induction medium consisted of CDM, 2 ng/ml TGF-β1 (100-21C, PeproTech), and 10 ng/ml PDGF-BB (100-14B, PeproTech).

Cardiac neural crest (CNC) cell differentiation was performed as follows. On day 0, ~80% confluent hPSCs were dissociated and seeded at a density of 2×10^4 cells/cm² onto new Matrigel- coated 6-well plates in StemMACS iPS-Brew XF medium ("Brew") (130-104-368, Miltenyi Biotec) + $10 \mu M$ Y-27632 (HY-10583, MedChem Express). On days 1 to 4, NC induction medium was added and changed daily. On days 5 and 6, NC induction medium + 1 µM retinoic acid (R2625, Sigma-Aldrich) was added daily. On day 7, cells were dissociated and split 1:6 in NC maintenance medium + 1 μ M retinoic acid + 10 μ M Y-27632. On days 8 and 9, NC maintenance medium + 1 μM retinoic acid was refreshed daily. On day 10, cells were dissociated and split 1:6 on gelatin (G1393, Sigma-Aldrich)-coated 6-well plates at a density of 2×10^4 cells/cm². NC maintenance medium was refreshed every day and cells were passaged when they reached ~90% confluency. From days 11 to 21, SMC induction medium was refreshed daily. On days 22 to 28, cells were maintained in Medium 231 (M231500, Thermo Fisher Scientific) + Smooth Muscle Growth Supplement (SMGS) (S00725, Thermo Fisher Scientific). Media which was refreshed every 2 days and cells were split 1:2 when they became confluent.

cVO differentiation

See Fig. 2C; fig. S3, C and D; and table S1 for an overview of our strategy and 34 CV differentiation screening conditions to produce cVOs. The Control groups utilized only CHIR, FGF2, and IWR. To begin, hPSCs suspended in single cells were transferred to Matrigel-coated non-micropatterned or micropatterned surfaces as described above and differentiated in RPMI-1640 media (61870036, Thermo Fisher Scientific) supplemented with B27 without insulin (A1895601, Thermo Fisher Scientific) (RB-I). The CV differentiation was based on the baseline differentiation described previously (3, 92) to promote CM differentiation and contained several additional small molecules and growth

factors to promote simultaneous endothelial and smooth muscle cell co-differentiation. On day 0, for primarily mesoderm induction (93), basal medium was supplemented with 4 or 5 μ M CHIR (S2924, Selleck Chemicals) and 5 ng/ml FGF2 (100-18B, PeproTech). On day 3, for CM induction, 5 μ M IWR (S7086, Selleck Chemicals) was added.

On days 5 to 16, to simultaneously induce endothelial cell vasculogenesis and angiogenesis (6, 56, 58, 59) along with the cardiomyocyte differentiation, we added combinations of 50 ng/ml VEGF (days 5, 7, 9, 11, 13, 15) (100-20, PeproTech); 5 ng/ml FGF2 (days 7, 9, 11, 13, 15) (100-18B, PeproTech); 10 μ M SB (days 7, 9, 11) (S1067, Selleck Chemicals); 50 ng/ml ANG2 (days 5, 7) (130-07, PeproTech); 50 ng/ml ANG1 (days 9, 11) (130-06, PeproTech); and select components of the VascuLife VEGF LifeFactors Kit (94) (LS-1020, Lifeline Cell Technology) (days 5, 7, 9, 11, 13, 15) (5 ng/ml EGF, 15 ng/ml IGF-1, 50 μ g/ml ascorbic acid, 0.75 U/ml heparin sulfate, 1 μ g/ml hydrocortisone).

On days 7 to 16, to simultaneously induce smooth muscle cell differentiation (7, 57) with cardiomyocyte and endothelial cell differentiation, we added 2.5 or 10 ng/ml PDGF-BB (days 7, 9, 11, 13, 15) (100-14B, PeproTech) and 0.5 or 2 ng/ml TGF- β 1 (days 7, 9, 11, 13, 15) (100-21C, PeproTech).

From days 5 to 16, unless otherwise noted, the basal medium was changed to contain B27 with insulin (RB+I) (17504044, Thermo Fisher Scientific) and was replaced every 48 hours thereafter. CMs within Control and cVO groups generally began spontaneously beating sometime between days 7 and 10. Cells were collected at various time points between days 0 and 16 for further downstream studies.

For spherical "3D" cVO creation, two methods were used. In the first method, to increase throughput and eliminate using stencils, each well of a black 96-well plate (M0562-32EA, Sigma- Aldrich) was freshly coated with a central, 2-µl drop of Matrigel (1:400 dilution) and was then seeded with a total of 125,000 hESC-3R cells. Cells were allowed to attach and grow for 2 to 4 days forming a single, homogenous, round colony in the center of each well. The same differentiation protocol for cVOs created from monolayer "2D" micropatterns was then used to create more spherical "3D" cVOs from days 0 to 14, using a range of CHIR from 6.0 to 8.5 μM . In the second method, we adapted our differentiation protocol to a "2D-to-3D" protocol recently used to create multi-chamber cardioids (34).

hVO differentiation

See Fig. 7A; fig S15, A and B; and table S5 for an overview of our strategy and hepatovascular (HV) differentiation to produce hVOs. We tested three differentiation conditions as follows: (i) Control (day 20 baseline hepatic differentiation, with no vascularization factors added); (ii) hVO-D3 (day 20 hVOs created by adding vascularization factors at day 3 of differentiation); and (iii) hVO-D6 (day 20 hVOs created by adding vascularization factors at day 6 of differentiation). To begin, hPSCs suspended in single cells were transferred to Matrigel-coated micropatterned surfaces as described above and differentiated in DMEM/F-12 media with GlutaMAX supplement (10565042, Thermo Fisher Scientific) supplemented with 0.5 mg/500 ml media of PVA (P8136, Sigma-Aldrich), 1x Insulin-Transferrin-Selenium (ITS) (41400045, Thermo Fisher Scientific), 1x chemically defined lipid concentrate (11905031, Thermo Fisher Scientific), 20 µl/500 ml media of 1-thioglycerol (M6145, Sigma-Aldrich), and 1x non-essential amino acids (NEAA) (11140050, Thermo Fisher Scientific). The hVO differentiation was based on the baseline differentiation described previously (4, 79) to promote hepatic differentiation and contained concentrations of the small molecules and growth factors found to promote simultaneous endothelial and smooth muscle cell production from the results of our cVO differentiation method above. On day 0, for mesendodermal induction, basal medium was supplemented with 100 ng/ml Activin-A (ActA) (338-AC, R & D Systems), 10 ng/ml BMP-4 (BMP4) (314-BP, R & D Systems), 3 μM CHIR (S2924, Selleck Chemicals), 100 ng/ml FGF2 (100-18B, PeproTech) and 10 µM LY294002 (LY) (70920, Cayman Chemical Company). On

Science 5 JUNE 2025 16 of 22

day 3, for foregut induction, 50 ng/ml FGF-10 (FGF10) (100-26, PeproTech) was used. On day 6, for hepatoblast induction, 10 ng/ml FGF10 and 10 ng/ml BMP-4 was used. Finally, to induce HCs, 50 ng/ml Hepatocyte Growth Factor (HGF) (100-39H, PeproTech), 50 ng/ml Oncostatin-M (OncoM) (300-10, PeproTech), and 10 μ M Dexamethasone (DEX) (1126, Tocris) was used.

Starting on days 3 or 6 and continuing until day 20, to simultaneously induce endothelial cell vasculogenesis and angiogenesis (6,56,58,59,94) along with the hepatocyte differentiation, we added combinations of 50 ng/ml VEGF (days 3 or 6, 9, 11, 13, 15, 17, and 19) (100-20, PeproTech); 5 ng/ml FGF2 (days 6 or 9, 11, 13, 15, 17, and 19) (100-18B, PeproTech); 10 μ M SB (days 6 or 9, 11, 13, 15, 17, and 19) (S1067, Selleck Chemicals); 50 ng/ml ANG2 (days 3 or 6, and 9) (130-07, PeproTech); 50 ng/ml ANG1 (days 11 and 13) (130-06, PeproTech); and select components of the VascuLife VEGF LifeFactors Kit (LS-1020, Lifeline Cell Technology) (days 3 or 6, 9, 11, 13, 15, 17, and 19) (5 ng/ml EGF, 15 ng/ml IGF-1, 50 μ g/ml ascorbic acid, 0.75 U/ml heparin sulfate, and 1 μ g/ml hydrocortisone).

On days 6 to 20, to simultaneously induce smooth muscle cell differentiation (7, 57) with hepatocyte and endothelial cell differentiation, we added 2.5 ng/ml PDGF-BB (days 6, 9, 11, 13, 15, 17, and 19) (100-14B, PeproTech) and 0.5 ng/ml TGF- β 1 (days 15, 17, and 19) (100-21C, PeproTech).

From days 3 to 9, the basal medium was changed to contain B27 with insulin (17504044, Thermo Fisher Scientific) (RB+I) and was replaced every 48 hours. From days 9 to 20, the basal medium was changed to HCM medium (CC-3198, Lonza) and was replaced every 48 hours. Cells were collected on day 20 for endpoint analyses.

Time-lapse microscopy

Initial time-lapse microscopy was performed with the Incucyte S3 Live-Cell Analysis Instrument (Essen Bioscience). Twenty-four-well plates containing a single 2-, 4-, or 6-mm circular micropattern of undifferentiated hESC-TNNT2-GFP cells (H9-hTnnT2-pGZ-TD2, WiCell) (52) in the center of each well were subjected to the baseline cardiomyocyte differentiation condition and imaged at 10 timepoints from days 0 to 9 (D0 to D9). Phase contrast and GFP signals were obtained with a 4x objective in a square mosaic containing the entire surface area of each well. At all time-points, plates were kept at 37°C and 5% $\rm CO_2\cdot$

To increase throughput, screening time-lapse microscopy was performed with the Cytation 5 Cell Imaging Multi-Mode Reader (BioTek). Five 48-well plates (204 out of 240 wells) were imaged over the differentiation time-period. The plates contained a single 2-mm circular micropattern of undifferentiated hESC-3R cells in the center of each well subjected to 34 differentiation conditions, with nominally four to six replicates per condition, imaged at six timepoints [days 3, 5, 8, 10, 12, and 16 (D3 to D16)].

Phase contrast, CFP, GFP, and mOrange signals in four independent channels were obtained and the following excitation light emitting diodes (LEDs), excitation (Ex) filters, emission (Em) filters, and dichroic (Di) mirrors were used for the fluorescence channels: CFP: LED-465 nm, Ex-445/45 nm, Em-510/42 nm, Di-482 nm; GFP: LED-465 nm, Ex-469/35 nm, Em-525/39 nm, Di-497 nm; mOrange: LED-523, Ex-531/40 nm, Em-593/40 nm, Di-568 nm. Light intensity and exposure time were adjusted for each channel to minimize under- or overexposure. A 4x objective (NA 0.13) was used to acquire a 4 by 4 array in a single focal plane for all channels, resulting in a rectangular mosaic containing the circular micropattern of cells and an area surrounding each micropattern which allowed imaging of migrating cells off each micropattern over time. At all time-points, plates were kept at 37°C and 5% CO₂ while imaging.

When using 48-well plates to screen 34 conditions and six replicates per condition, the number of wells needed was 204. Therefore, the theoretical number of acquired raw images was 78,336 images (16 images/channel/mosaic \times 4 channels/mosaic \times 6 days/well \times 204 wells/day). The actual number of acquired raw images was 75,648, corresponding to 197 wells (out of 204 wells), with 7 wells excluded

because of debris, detachment of micropatterns, and incomplete micropatterns at the start of differentiation (representing 3.4% exclusion of wells).

After all raw images were acquired, image analysis was performed with Gen5 v3.05 software (BioTek). Images in each channel and each 4 by 4 array were stitched to create a single mosaic image; 4728 mosaics were created, and each mosaic image was downsized by 25%. Next, image processing of each mosaic was performed to reduce background independently in each channel. Finally, for each channel, thresholding was performed on fluorescence intensity along with minimum and maximum object size to calculate the total Phase, CFP, GFP, and morange total fluorescence area in each well for each condition at each time-point. Each mosaic image was computationally masked by a circular "plug" to eliminate fluorescence artifact created by well edges. For each condition, values for replicate samples were summed, and the mean and standard deviation were calculated.

Widefield microscopy

Either an AxioObserver Z1 (Zeiss) or a Keyence BZ-X700 (Keyence) inverted microscope was used to visualize undifferentiated hPSCs and their derivatives. The Zeiss microscope was equipped with 2.5x, 4x, 10x, 20x, 40x, and 63x objectives, a Lambda DG-4 300 W Xenon light source (Sutter Instruments), an ORCA-ER CCD camera (Hamamatsu) to visualize Phase, CFP, GFP, and mOrange channels, and ZEN (Blue Edition) v3.9 software (Zeiss) for image stitching, z-stack image capturing, and incubation control. The Keyence microscope was equipped with 2x, 4x, 10x, and 20x objectives, an 80-W metal halide lamp, a monochrome CCD camera to visualize Phase, CFP, GFP, and mOrange channels, and BZ-X Analyzer software for optical sectioning, image stitching, z-stack image capturing, and incubation control. Both microscope incubation systems were maintained at 37°C and 5% CO₂-

Confocal microscopy

Either a Zeiss Airyscan 2 LSM980 Plus NIR Inverted Confocal Microscope (Carl Zeiss) (Stanford Neuroscience Microscopy Service Core Facility) or a Leica SP8 White Light Confocal (Leica) (Stanford Cell Sciences Imaging Core Facility) confocal microscope was used to visualize live and fixed undifferentiated hPSCs, individual hPSC-derived cells, and cVOs. The Zeiss LSM980 confocal (AxioObserver Z1 inverted microscope base) is equipped with the following: environmental chamber to maintain samples at 37°C and 5% CO2; motorized X-Y stage and Z focus; 10x Plan Apochromat (NA 0.45); 20x Plan Apochromat (NA 0.45); 40x Plan Neofluar (oil) (NA 1.30); 63x Plan Apochromat (oil) (NA 1.40); 405-nm diode laser (30 mW); 458-/488-/514-nm argon laser (35 mW); 561-nm diode-pumped solid-state (DPSS) laser (20 mW); 633-nm helium-neon (HeNe) laser (5 mW); temperature-stabilized VIS-acousto-optical tunable filter (AOTF) for simultaneous intensity control; and Zeiss ZEN Blue v3.9 software. The Leica SP8 confocal (DMI 6000 inverted microscope platform) is equipped with the following: environmental chamber to maintain samples at 37°C and 5% CO₂; motorized X-Y stage and galvanometer Z focus; 10x Plan Apochromat (NA 0.40); 20x Plan Apochromat (oil) (NA 0.75); 40x Plan Apochromat (oil) (NA 1.30); 63x Plan Apochromat (oil) (NA 1.40); 405-nm laser (50 mW); super continuum, white light (WLL) pulsed laser (avg. power 1.5 mW), 470 nm to 670 nm, 78 MHz; acoustical optical beam splitter (AOBS) for selection of up to eight discrete laser lines (1-nm precision); three hybrid-GaAsP detectors; two standard fluorescent photomultiplier tubes (PMT); and Leica LAS AF software. Offline image analysis was also performed with Zeiss ZEN Blue v3.9 software to stich mosaic-acquired images, to apply LSM Plus linear Wiener filter deconvolution, and to create MIP images of confocal image stacks. Imaris v10.1.1 software was used to create 3D surface renderings and quantify vascular characteristics. ImageJ (Fiji) v2.14.0 software was used to create regions of interest (ROIs) and to quantify total fluorescence areas.

Science 5 JUNE 2025 17 of 22

Immunocytochemistry (ICC)

Primary and secondary antibodies (table S7) were reconstituted in sterile PBS per manufacturer guidelines. Monolayer samples were fixed in IC Fixation Buffer (FB001, Thermo Fisher Scientific, diluted in PBS) or 4% paraformaldehyde (15713S, Electron Microscopy Sciences) for 10 to 15 min and washed with PBS for 10 min three times; cVOs and hVOs were fixed for 30 min. To begin staining, samples were permeabilized with 0.1% Triton-X for 30 min at room temperature and then incubated in blocking buffer (10% normal goat serum and 0.05% Tween in PBS) or BlockAid (B10710, Thermo Fisher Scientific) for 1 hour at room temperature. Then the primary antibody (prepared in blocking buffer or BlockAid) was applied overnight at 4°C for monolayers or for 24 to 48 hours at room temperature for cVOs and hVOs. Washing buffer (0.05% Tween in PBS) was applied to the samples for 5 min at room temperature three times. Secondary antibody (typically at 1:500 dilution) was applied for 1 hour at room temperature for monolayers or for 24 to 48 hours at room temperature for cVOs and hVOs, followed by three 5-min washes in wash buffer. After a final 5-min rinse with sterile PBS, samples were counterstained with either DAPI (D8417, Sigma), DRAQ5 Fluorescent Probe Solution (62251, Thermo Fisher Scientific), or Hoechst 33342 (H3570, Thermo Fisher Scientific). Samples were either analyzed immediately or stored at 4°C in PBS.

Bulk RNA-sequencing (bRNA-seq)

hESC-3R (1 group, day 0, n=3, 3 total samples; note, these samples were used for both cardiac and hepatic analyses), Control, and cVO samples (2 groups, days 2, 5, 8, 10, 12, and 16, n=3 per sample, 36 total samples) were prepared with the Direct-zol RNA Microprep w/ Zymo- Spin IC Columns (R2060, Zymo Research) and sequenced. For hVO analysis, Control, hVO-D3, and hVO-D6 samples (three groups, day 20, n=3 per sample, nine total samples) were prepared in the same fashion. Each replicate had an average of 24.4 million 150-bp-long paired-end reads. FastQC v0.11.2 was used for sequencing quality assessment. Reads were then aligned to the GRCh38 (hg38) reference genome using STAR v2.5.3a with splice junctions being defined in GTF file (obtained from GRCh38). An average of 85.3% of reads was aligned to the reference transcriptome.

Expression at the gene level was determined by read counts using RSEM 1.2.30. Differently expressed genes (DEGs) with fold-change were further detected by DEseq2 version 1.10.1 for comparable conditions. Based on the DEG data set, the Euclidean distances between samples, as calculated from the rlog transformation, were calculated and plotted as a heatmap.

To determine heatmap scale, the following was performed. After hierarchical clustering using Median Clustering or the Weighted Pair Group Method with Median Clustering (WPGMC) method together with the Spearman correlation (square of Euclidean distance) method for distance measurement on the log-transformed gene expression table, the values were further scaled in the row direction. This centers and standardizes each row separately to row Z-score.

PCA was performed to extract the main information from the DESeq2 transformed (rlog) data set so that each successive axis was ordered by decreasing order of variance. Approximately 60% of all transcripts (15,994 of 26,470 total genes) after minimal pre-filtering to keep only rows which contained at least 10 total read/raw counts were used for PCA. PCA plots were used to visualize the batch effects and overall effect of experimental covariates. Numbers on each plot axis indicate frequency of transcripts described by each principal component.

WGCNA was used for hierarchical clustering with dynamic tree cut to identify gene co-expression modules; the modules were further analyzed using IPA (Qiagen), described below. RNA-seq data of hESC, Control, cVO, and hVO samples are deposited in the NIH Gene Expression Omnibus (GEO) under GSE185194.

ΙΡΔ

We used IPA (v65367011, Qiagen) of the temporal bRNA-seq WGCNA of Control and cVO samples to show vascularization and cardiogenesis regulator effect networks. In addition, we used IPA to show predicted top canonical pathways, upstream regulators, functions, regulator effect networks, and networks of day 16 cVOs compared to D16 Control samples. WGCNA Module 16 (Pale Turquoise) within the "Vascularization Genes" cluster (Fig. 4I) contained 1258 analysis-ready genes with a Log2FoldChange ranging from -0.9 to 15.1 (13 down-regulated and 1245 up-regulated genes) and revealed regulator effect networks related to vascularization. WGCNA Module 12 (Dark Grey) within the "Cardiomyocyte/Endothelial/Smooth Muscle/Fibroblast Genes" cluster (Fig. 4I) contained 3719 analysis-ready genes with a Log2FoldChange ranging from -1.2 to 17.8 (46 down-regulated and 3673 up-regulated genes) and revealed regulator effect networks related to cardiogenesis. For analysis of day 16 cVOs compared to D16 Control samples, 15,671 differentially expressed genes (Log2FoldChange ranging from -7.2 to 8.3) were reduced to 1001 analysis-ready genes by analyzing only differentially expressed genes with Log2FoldChange cutoff values of below -2 and above +2 and padj value ≥ 0.05 .

scRNA-seq

cVO samples (day 16, n=6 pooled organoids per sample) were dissociated using the Pierce Primary Cardiomyocyte Isolation Kit (88281, Thermo Fisher Scientific) according to the manufacturer's instructions. A 10-µl sample of dissociated single cells was visualized with a fluorescent microscope (Zeiss) to verify the presence of GFP⁺, mOrange⁺, and CFP⁺ cells in the sample. Next, single cells (with an end-target of ~5000 cells per sample) were used to create Gel Bead-In EMulsions (GEMs) by using the Chromium Single Cell 3' Library & Gel Bead Kit v2 kit (PN-120267, 10X Genomics). Libraries were generated according to the manufacturer's instructions and sequenced using the HiSeq2500 instrument (Illumina) with a read length of PE150 base pairs at each end and ~50 M reads per sample.

Sequences were demultiplexed into FASTQ files using Cell Ranger 3.0.0 (l0X Genomics) and then aligned to the GRCh38 (hg38) reference genome. Count matrices were generated using the count function with default settings. Results were initially visualized with Loupe Cell Browser v8 (10X Genomics) and then detailed downstream analysis was performed with the Seurat package (v.5.1.0) (60) in RStudio (v1.4.1106, RStudio) using R (v3.6.1 and 4.0.4, R Core).

Barcodes, features (genes), and matrix files of cVOs 1 to 3 were loaded into RStudio as a Seurat objects using CreateSeuratObject with a minimum of five cells and 200 genes, and percent mitochondrial genes were identified. Cells with greater than 200 and less than the top 1% genes, and mitochondrial content less than 10% were analyzed. We first performed SCTransform normalization according to the Seurat "SCTranform Vignette". Next, RunPCA was used to perform linear dimensional reduction by PCA. ElbowPlot identified an 'elbow' at various principal components. Non-linear dimensional reduction was performed using RunUMAP. Clustering was performed using FindNeighbors and FindClusters typically using 30 principal component dimensions and 0.152 resolution. Uniform Manifold Approximation and Projection (UMAP) plots were visualized using DimPlot.

Finally, DEGs were identified with FindAll Markers and violin, feature plots, and heat maps were visualized with VlnPlot, FeaturePlot, and DoHeatmap. Cell-type annotations for each cluster were assigned using the Azimuth human adult scRNA-seq reference set (62–64) (table S2). scRNA-seq data of Control and cVO samples are deposited in the NIH GEO under GSE185194.

scRNA-seq public data, integration with cVOs, and annotation

The scRNA-seq data from a 6.5-PCW human embryonic heart were described by Asp *et al.* (45) and re-analyzed by Ameen *et al.* (61). Count

Science 5 JUNE 2025 18 of 22

matrix and meta data were loaded into RStudio as a Seurat object using CreateSeuratObject with a minimum of five cells and 200 genes, and percent mitochondrial genes were identified. Cells with greater than 200 and less than the top 1% genes, and mitochondrial content less than 10% were analyzed. We first performed SCTransform normalization according to the Seurat "SCTranform Vignette". Next RunPCA was used to perform linear dimensional reduction by PCA. ElbowPlot identified an 'elbow' at various principal components (PCs). Non-linear dimensional reduction was performed using RunUMAP. Clustering was performed using FindNeighbors and FindClusters typically using 30 principal component dimensions and 0.25 resolution. UMAP plots were visualized using DimPlot.

After loading and processing cVO and 6.5-PCW samples separately, they were merged using Merge, and SCTransform was used to run an unintegrated analysis. Next, anchor-based CCA integrative analysis was performed using IntegrateLayers and the CCAIntegration method according to the Seurat "Integrative Analysis Vignette". FindNeighbors, FindClusters, RunUMAP, and DimPlot were then run on the integrated data.

After integration, we joined layers using JoinLayers and then loaded the Azimuth human adult scRNA-seq reference set (62-64) using RunAzimuth to compare cell types from cVOs 1 to 3 and 6.5-PCW samples. We annotated clusters with the "Celltype.L2" annotations (table S2). For differential gene expression we first ran PrepSCTFindMarkers then FindAllMarkers. We then visualized composite or individual sample gene expression using DoHeatMap and VlnPlot.

Cell-cell communication analysis

As we have previously described (53), to quantify the putative cell-cell communication in the cardiovascular cellulome, we obtained human ligand-receptor pairs compiled by Ramilowski *et al.* (95). Briefly, we defined a ligand or receptor as "expressed" in a particular cell type if its expression is higher than 0 in more than 10% of cells in that cell type for the gene encoding the ligand or receptor. We linked any two cell types where the ligand was expressed in the former cell type and the receptor in the latter to define networks of cell-cell communication. The directionality in this relationship is visible where lines connecting cell populations are colored according to the population broadcasting the ligand and connect via an arrowhead to the population expressing the receptor, thus demonstrating a capability to receive the signal. In addition, line thickness correlates with the interaction number. To plot networks, we used the igraph and circlize R packages.

NO testing

To determine the NO producing ability of hPSC-ECs in cVOs, we used the Nitric Oxide (total) detection kit (ADI-917-020, Enzo). The enzymatic conversion of nitrate to nitrite by nitrate reductase, followed by the Griess reaction to form a colored azo dye product, allowed assessment of NO produced by the hPSC-ECs. Quantification of NO produced was achieved by measuring absorption at 540-570 nm with the use of the Cytation 5 Cell Imaging Multi-Mode Reader (BioTek), averaged from four independent experiments.

Electrical stimulation

For electrical stimulation studies, multi-well plates containing Control or cVO samples were placed in a customized upright optical imaging system (121517T1UP, SciMedia) and paced in Tyrode's solution (T2397, Sigma). Samples were then point stimulated with a stimulus generator (SIU-102, Warner Instruments). The electrical stimulation consisted of a biphasic waveform with peak-to-peak amplitude of 5 to 10 V, pulse width of 2 to 5 ms, and frequency of 1 or 2 Hz; point stimulation was delivered through a custom-made 1-mm two-wire platinum anode/ cathode electrode.

MEA EP

Controls and cVOs were differentiated as described above. For MEA EP, spontaneously beating organoids were detached from the culture plates using blunt-ended Pasteur glass pipettes to keep the organoids intact. This was done under a stereomicroscope fitted in a cell culture hood. For field potential recordings, 48-well MEA plates (M768-tMEA-48W, Axion Biosystems) were coated with Matrigel (356231, Corning) (1:50) or fibronectin (50 μg/ml) (F1141-2MG, Sigma-Aldrich) at 37°C for 1 hour. The detached organoids were transferred to the MEA plate using a 200-µl pipette tip with a large bore, placing one organoid per well in at least 50 to 100 μl of RPMI/B27 media for Controls or vascular induction media for cVOs. The organoids were placed on top of the recording electrodes and carefully transferred to the incubator, allowing the organoids to attach overnight without disturbance. Intrinsic field potential recordings were performed 4 days after plating the organoids using the Maestro Pro Multi-well MEA System (Axion Biosystems). Data were analyzed using a custom-made MATLAB (vR2024a, MathWorks) program.

Sharp electrode EP

Organoids were detached from their culture plates as described in the MEA EP section above. Next, five to six organoids were transferred to 35-mm glass-bottom dishes (D35-20-1.5-N, Cellvis) coated with 1:50 Matrigel in RPMI/B27 for 1 hour at 37°C. The organoids were allowed to attach overnight at 37°C and were maintained by changing the media every other day. For intrinsic action potential recordings, the organoids were incubated with RPMI/B27 (Controls) and vascular induction media (cVOs) containing 10 µM blebbistatin (B0560-5MG, Sigma-Aldrich) for 45 to 60 min at 37°C. Subsequently, the media was replaced with Tyrode solution, and the dish was transferred to an electrophysiology rig with a heating platform. Action potentials were recorded from the organoids using the HEKA EPC10 USB amplifier and HEKA PATCHMASTER data acquisition software. Filamented borosilicate glass electrodes (BF100-50-10, Sutter Instruments) were pulled using a P1000 pipette puller (Sutter Instruments) to produce pipettes with a tip resistance of 35 to 50 $M\Omega$ when filled with a 3 M KCl (529552, Sigma-Aldrich) pipette solution. Using these sharp electrodes, the organoids were impaled, and membrane potentials were recorded. All experiments were conducted at 37°C, with the bath temperature maintained using a Warner Instruments temperature controller unit (Harvard Apparatus). All data were analyzed using a custom-made MATLAB (vR2024a, MathWorks) program. Action potentials were classified into atrial-like or ventricular-like based on their morphological features and specific quantitative criteria. Ventricular CMs typically exhibit a longer action potential with a pronounced plateau phase, while atrial CMs display a shorter action potential with a steeper repolarization phase. The shape and duration of the action potential are used to differentiate between these cell types. Additionally, the ratio (APD90c-APD50c)/APD90c, was used as a quantitative measure to classify the cells: a ratio of ≤0.15 is indicative of ventricular CMs, while a ratio of >0.15 is indicative of atrial CMs.

Calcium dye imaging (CDI)

For CDI, the Fluo-4 Direct Calcium Assay kit was used (F10471, Thermo Fisher) as per the manufacturer's instructions as previously described (15). Briefly, Fluo-4 loading solution was incubated with the samples at 37°C for 30 min, washed twice with HBSS (14025092, Thermo Fisher), and resuspended Tyrode's solution. Fluorescence was measured at 495 \pm 20 nm excitation and 515 \pm 20 nm emission. Videos were taken with an Evolve 512 Delta EMCCD camera (Photometrics) using Micromanager v1.4 software (Vale Lab, UCSF) at 90 fps for 10 s of Control or cVO samples beating spontaneously or electrically stimulated at 1 or 2 Hz. In each video frame, ROIs were analyzed for changes in dye intensity f/f0, with the resting fluorescence value f0 determined at the first frame of each video. Background intensity was subtracted

Science 5 JUNE 2025 19 of 22

RESEARCH ARTICLE

from all values, and plots were normalized to zero. BV-Ana software (SciMedia) was used to quantify conduction velocity and beating frequency.

Contractility imaging

We assessed the contractility of Control and cVO groups in a similar manner as we have previously described (96). Contraction of beating CMs within the micropatterns was recorded with high-resolution motion capture tracking (75 fps) using the SI8000 Live Cell Motion Imaging System (Sony Corporation). During data collection, cells were maintained under controlled humidified conditions at 37°C with 5% CO₂ and 95% air in a stage-top microscope incubator (Tokai Hit). Functional parameters were assessed from the averaged contraction-relaxation waveforms from 10-s recordings, using the SI8000C Analyzer software (Sony Corporation). The software was used to detect motion vectors and quantify beating rate, contraction velocity, relaxation velocity, and contraction-relaxation peak interval of cVOs. Alternatively, we obtained videos of contracting Control and cVO groups using our climate-controlled Cytation 5 Cell Imaging Multi-Mode Reader (BioTek) and then quantified contraction characteristics using MUSCLEMOTION (97).

Microsphere vascular lumen identification

For vascular lumen identification, either dark red (Ex/Em 660/680 nm) 0.2- μ m FluoSpheres carboxylate-modified microspheres (2% v/v) (F8807, Thermo Fisher Scientific), or crimson (Ex/Em 625/645 nm) 1.0- μ m FluoSpheres carboxylate-modified microspheres (F8816, Thermo Fisher Scientific), or blue (Ex/Em 365/447 nm) 1.0- μ m Fluoro-Max dyed aqueous fluorescent particles (B0100, Thermo Fisher Scientific) were diluted 1:1000 in culture medium (RPMI+B27), then added to live cVOs and incubated at 37°C and 5% CO₂ on a rocker at 15 rpm for 1 hour. cVOs were then rinsed with culture medium three times before confocal imaging with appropriate laser excitation and fluorescence detection to detect microspheres within cVO vascular lumen.

Signaling pathway inhibition

For NOTCH signaling pathway inhibition we used 0, 1, and 10 μM DAPT (GSI-IX) (S2215, Selleck Chemicals) added at day 0 of differentiation. For BMP signaling pathway inhibition, we used 0, 0.1, and 1 μM Dorsomorphin (P5499, Sigma-Aldrich) added at day 0 of differentiation.

Teratogen drug testing

For teratogen drug testing, we used 0 and 10 nM of fentanyl added at day 0 of differentiation.

Statistical analysis

Statistical analyses were performed using Prism 10 (GraphPad Software, LLC) and JMP Pro 15 (SAS Institute, Inc.) software. Data was first analyzed for normality and lognormality using the D'Agostino & Pearson, Anderson-Darling, Shapiro-Wilk, and Kolmogorov-Smirnov tests in Prism 10. If data comprised two normally distributed groups, a parametric unpaired two-tailed Student's t test was performed to determine significant differences. If data comprised two non-normally distributed groups, a nonparametric two-tailed Wilcoxon/Mann-Whitney U test was performed. If data comprised greater than two normally distributed groups, a parametric one-way or two-way ANOVA was performed. If data comprised greater than two non-normally distributed groups, a nonparametric Kruskal-Wallis test was performed. Subsequent multiple comparisons correction analysis was performed using the parametric Tukey's or Šídák's test for normally distributed data and the nonparametric Dunn's test for non-normally distributed data. Data are expressed as mean \pm standard deviation (SD). The P values for significance differences are as follows: *P < 0.05, **P < 0.005, ***P < 0.0005, ****P < 0.0005, ****P < 0.0005, ****P < 0.0005, *****P < 0.0005, ****P < 0.0005, *****P < 0.0005, ****P < 0.0005, ****P < 0.0005, *****P < 0.00050.00005, not significant (ns). Statistical methods were not used to predetermine sample size. Samples were randomized with respect to applied differentiation conditions and assays. The investigators were not blinded to samples, experiments, and assessments of outcome. Detailed information regarding sample size, statistical analyses, and statistical significance is included in each figure.

REFERENCES AND NOTES

- J. A. Thomson et al., Embryonic stem cell lines derived from human blastocysts. Science 282, 1145–1147 (1998). doi: 10.1126/science.282.5391.1145; pmid: 9804556
- K. Takahashi et al., Induction of pluripotent stem cells from adult human fibroblasts by defined factors. Cell 131, 861–872 (2007). doi: 10.1016/j.cell.2007.11.019; pmid: 18035408
- P. W. Burridge et al., Chemically defined generation of human cardiomyocytes. Nat. Methods 11, 855–860 (2014). doi: 10.1038/nmeth.2999; pmid: 24930130
- Y. Guan et al., Human hepatic organoids for the analysis of human genetic diseases. JCI Insight 2, e94954 (2017). doi: 10.1172/jci.insight.94954; pmid: 28878125
- A. Caudal, M. P. Snyder, J. C. Wu, Harnessing human genetics and stem cells for precision cardiovascular medicine. *Cell Genom.* 4, 100445 (2024). doi: 10.1016/j.xgen.2023.100445; pmid: 38359791
- D. James et al., Expansion and maintenance of human embryonic stem cell-derived endothelial cells by TGFbeta inhibition is Id1 dependent. Nat. Biotechnol. 28, 161–166 (2010). doi: 10.1038/nbt.1605; pmid: 20081865
- C. Cheung, A. S. Bernardo, M. W. Trotter, R. A. Pedersen, S. Sinha, Generation of human vascular smooth muscle subtypes provides insight into embryological origin-dependent disease susceptibility. *Nat. Biotechnol.* 30, 165–173 (2012). doi: 10.1038/nbt.2107; pmid: 22252507
- M. Shen, C. Liu, J. C. Wu, Stem Cell Assays: Methods and Protocols, N. Kannan, P. Beer, Eds. (Springer US, 2022), pp. 233–246.doi: 10.1007/978-1-0716-1979-7_15
- M. Shen et al., Protocol to generate cardiac pericytes from human induced pluripotent stem cells. STAR Protoc. 4, 102256 (2023). doi: 10.1016/j.xpro.2023.102256; pmid: 37119139
- H. Zhang et al., Generation of quiescent cardiac fibroblasts from human induced pluripotent stem cells for invitro modeling of cardiac fibrosis. Circ. Res. 125, 552–566 (2019). doi: 10.1161/CIRCRESAHA.119.315491; pmid: 31288631
- T. Neri et al., Human pre-valvular endocardial cells derived from pluripotent stem cells recapitulate cardiac pathophysiological valvulogenesis. Nat. Commun. 10, 1929 (2019). doi: 10.1038/s41467-019-09459-5; pmid: 31028265
- X. Bao et al., Long-term self-renewing human epicardial cells generated from pluripotent stem cells under defined xeno-free conditions. Nat. Biomed. Eng. 1, 0003 (2016). doi: 10.1038/s41551-016-0003; pmid: 28462012
- O. Caspi et al., Tissue engineering of vascularized cardiac muscle from human embryonic stem cells. Circ. Res. 100, 263–272 (2007). doi: 10.1161/01.RES.0000257776.05673.ff; pmid: 17218605
- E. Giacomelli et al., Three-dimensional cardiac microtissues composed of cardiomyocytes and endothelial cells co-differentiated from human pluripotent stem cells. *Development* 144, 1008–1017 (2017). doi: 10.1242/dev.143438; pmid: 28279973
- O. J. Abilez et al., Passive stretch induces structural and functional maturation of engineered heart muscle as predicted by computational modeling. Stem Cells 36, 265–277 (2018). doi: 10.1002/stem.2732; pmid: 29086457
- T. Takebe et al., Vascularized and functional human liver from an iPSC-derived organ bud transplant. Nature 499, 481–484 (2013). doi: 10.1038/nature12271; pmid: 23823721
- B. Palikuqi et al., Adaptable haemodynamic endothelial cells for organogenesis and tumorigenesis. Nature 585, 426–432 (2020). doi: 10.1038/s41586-020-2712-z; pmid: 32908310
- P. Guye et al., Genetically engineering self-organization of human pluripotent stem cells into a liver bud-like tissue using Gata6. Nat. Commun. 7, 10243 (2016). doi: 10.1038/ ncomms10243; pmid: 26732624
- M. A. Skylar-Scott et al., Orthogonally induced differentiation of stem cells for the programmatic patterning of vascularized organoids and bioprinted tissues. *Nat. Biomed. Eng.* 6, 449–462 (2022). doi: 10.1038/s41551-022-00856-8; pmid: 35332307
- B. Grigoryan et al., Multivascular networks and functional intravascular topologies within biocompatible hydrogels. Science 364, 458–464 (2019). doi: 10.1126/science.aav9750; pmid: 31048486
- M. A. Skylar-Scott et al., Biomanufacturing of organ-specific tissues with high cellular density and embedded vascular channels. Sci. Adv. 5, eaaw2459 (2019). doi: 10.1126/ sciadv.aaw2459; pmid: 31523707
- J. H. Low et al., Generation of human psc-derived kidney organoids with patterned nephron segments and a de novo vascular network. Cell Stem Cell 25, 373–387.e9 (2019). doi: 10.1016/j.stem.2019.06.009; pmid: 31303547
- A. A. Mansour et al., An invivo model of functional and vascularized human brain organoids. Nat. Biotechnol. 36, 432–441 (2018). doi: 10.1038/nbt.4127; pmid: 29658944
- R. A. Wimmer et al., Human blood vessel organoids as a model of diabetic vasculopathy.
 Nature 565, 505–510 (2019). doi: 10.1038/s41586-018-0858-8; pmid: 30651639
- F. B. Myers et al., Robust pluripotent stem cell expansion and cardiomyocyte differentiation via geometric patterning. *Integr. Biol.* 5, 1495–1506 (2013). doi: 10.1039/ c2ib20191g; pmid: 24141327

Science 5 JUNE 2025 20 of 22

- Z. Ma et al., Self-organizing human cardiac microchambers mediated by geometric confinement. Nat. Commun. 6, 7413 (2015). doi: 10.1038/ncomms8413; pmid: 26172574
- P. Hoang, J. Wang, B. R. Conklin, K. E. Healy, Z. Ma, Generation of spatial-patterned early-developing cardiac organoids using human pluripotent stem cells. *Nat. Protoc.* 13, 723–737 (2018). doi: 10.1038/nprot.2018.006; pmid: 29543795
- L. Drakhlis et al., Human heart-forming organoids recapitulate early heart and foregut development. Nat. Biotechnol. 39, 737–746 (2021). doi: 10.1038/s41587-021-00815-9; pmid: 33558697
- P. Hofbauer et al., Cardioids reveal self-organizing principles of human cardiogenesis. Cell 184, 3299–3317.e22 (2021). doi: 10.1016/j.cell.2021.04.034; pmid: 34019794
- Y. R. Lewis-Israeli et al., Self-assembling human heart organoids for the modeling of cardiac development and congenital heart disease. Nat. Commun. 12, 5142 (2021). doi: 10.1038/s41467-021-25329-5; pmid: 34446706
- 31. G. Rossi *et al.*, Capturing cardiogenesis in gastruloids. *Cell Stem Cell* **28**, 230–240.e6 (2021). doi: 10.1016/j.stem.2020.10.013; pmid: 33176168
- 32. A. C. Silva et al., Co-emergence of cardiac and gut tissues promotes cardiomyocyte maturation within human iPSC-derived organoids. *Cell Stem Cell* **28**, 2137–2152.e6 (2021). doi: 10.1016/j.stem.2021.11.007; pmid: 34861147
- Z. T. Olmsted, J. L. Paluh, A combined human gastruloid model of cardiogenesis and neurogenesis. iScience 25, 104486 (2022). doi: 10.1016/j.isci.2022.104486; pmid: 35721464
- C. Schmidt et al., Multi-chamber cardioids unravel human heart development and cardiac defects. Cell 186, 5587–5605.e27 (2023). doi: 10.1016/j.cell.2023.10.030; pmid: 38029745
- 35. M. Dardano *et al.*, Blood-generating heart-forming organoids recapitulate co-development of the human haematopoietic system and the embryonic heart. *Nat. Cell Biol.* **26**, 1984–1996 (2024). doi: 10.1038/s41556-024-01526-4; pmid: 39379702
- H. Koike et al., Modelling human hepato-biliary-pancreatic organogenesis from the foregut-midgut boundary. Nature 574, 112–116 (2019). doi: 10.1038/s41586-019-1598-0; pmid: 31554966
- R. Passier, V. Orlova, C. Mummery, Complex tissue and disease modeling using hipscs. Cell Stem Cell 18, 309–321 (2016). doi: 10.1016/j.stem.2016.02.011; pmid: 26942851
- N. F. Huang et al., Big bottlenecks in cardiovascular tissue engineering. Commun. Biol. 1, 199 (2018). doi: 10.1038/s42003-018-0202-8; pmid: 30480100
- J. Elisseeff, S. F. Badylak, J. D. Boeke, Immune and genome engineering as the future of transplantable tissue. N. Engl. J. Med. 385, 2451–2462 (2021). doi: 10.1056/ NEJMra1913421; pmid: 34936741
- K. Red-Horse, H. Ueno, I. L. Weissman, M. A. Krasnow, Coronary arteries form by developmental reprogramming of venous cells. *Nature* 464, 549–553 (2010). doi: 10.1038/nature08873; pmid: 20336138
- S. M. Meilhac, M. E. Buckingham, The deployment of cell lineages that form the mammalian heart. *Nat. Rev. Cardiol.* 15, 705–724 (2018). doi: 10.1038/s41569-018-0086-9; pmid: 30266935
- Hyun, A. Wilkerson, J. Johnston, Embryology policy: Revisit the 14-day rule. Nature 533, 169–171 (2016). doi: 10.1038/533169a; pmid: 27172031
- K. D. Wilson et al., Endogenous retrovirus-derived Incrna BANCR promotes cardiomyocyte migration in humans and non-human primates. Dev. Cell. 54, 694–709.e9 (2020). doi: 10.1016/j.devcel.2020.07.006; pmid: 32763147
- 44. R. O'Rahilly, F. Müller, G. L. Streeter, Carnegie Institution of Washington, *Developmental Stages in Human Embryos: Including a Revision Of Streeter's Horizons and a Survey of the Carnegie Collection* (Carnegie Institution of Washington, 1987), pp. 1–306.
- M. Asp et al., A spatiotemporal organ-wide gene expression and cell atlas of the developing human heart. Cell 179, 1647–1660.e19 (2019). doi: 10.1016/j.cell.2019.11.025; pmid: 31835037
- A. Warmflash, B. Sorre, F. Etoc, E. D. Siggia, A. H. Brivanlou, A method to recapitulate early embryonic spatial patterning in human embryonic stem cells. *Nat. Methods* 11, 847–854 (2014). doi: 10.1038/nmeth.3016; pmid: 24973948
- 47. A. Deglincerti et al., Self-organization of human embryonic stem cells on micropatterns.

 Nat. Protoc. 11, 2223–2232 (2016). doi: 10.1038/nprot.2016.131; pmid: 27735934
- I. Martyn, A. H. Brivanlou, E. D. Siggia, A wave of WNT signaling balanced by secreted inhibitors controls primitive streak formation in micropattern colonies of human embryonic stem cells. *Development* 146, dev172791 (2019). doi: 10.1242/dev.172791; pmid: 30814117
- I. Martyn, T. Y. Kanno, A. Ruzo, E. D. Siggia, A. H. Brivanlou, Self-organization of a human organizer by combined Wnt and Nodal signalling. *Nature* 558, 132–135 (2018). doi: 10.1038/s41586-018-0150-y; pmid: 29795348
- L. Yang et al., Human cardiovascular progenitor cells develop from a KDR+ embryonicstem-cell-derived population. Nature 453, 524–528 (2008). doi: 10.1038/nature06894; pmid: 18432194
- D. A. Elliott et al., NKX2-5(eGFP/w) hESCs for isolation of human cardiac progenitors and cardiomyocytes. Nat. Methods 8, 1037–1040 (2011). doi: 10.1038/nmeth.1740; pmid: 22020065
- P. J. Wrighton et al., Signals from the surface modulate differentiation of human pluripotent stem cells through glycosaminoglycans and integrins. Proc. Natl. Acad. Sci. U.S.A. 111, 18126–18131 (2014). doi: 10.1073/pnas.1409525111; pmid: 25422477

- D. T. Paik et al., Large-scale single-cell rna-seq reveals molecular signatures of heterogeneous populations of human induced pluripotent stem cell-derived endothelial cells. Circ. Res. 123, 443–450 (2018). doi: 10.1161/CIRCRESAHA.118.312913; pmid: 29986945
- 54. Y. Brudno, A. B. Ennett-Shepard, R. R. Chen, M. Aizenberg, D. J. Mooney, Enhancing microvascular formation and vessel maturation through temporal control over multiple pro-angiogenic and pro-maturation factors. *Biomaterials* 34, 9201–9209 (2013). doi: 10.1016/j.biomaterials.2013.08.007; pmid: 23972477
- K. M. Park, S. Gerecht, Harnessing developmental processes for vascular engineering and regeneration. *Development* 141, 2760–2769 (2014). doi: 10.1242/dev.102194; pmid: 25005471
- A. V. Shah et al., The endothelial transcription factor ERG mediates Angiopoietin-1dependent control of Notch signalling and vascular stability. Nat. Commun. 8, 16002 (2017). doi: 10.1038/ncomms16002; pmid: 28695891
- C. Patsch et al., Generation of vascular endothelial and smooth muscle cells from human pluripotent stem cells. Nat. Cell Biol. 17, 994–1003 (2015). doi: 10.1038/ncb3205; pmid: 26214132
- P. Saharinen, L. Eklund, K. Alitalo, Therapeutic targeting of the angiopoietin-TIE pathway.
 Nat. Rev. Drug Discov. 16, 635–661 (2017). doi: 10.1038/nrd.2016.278; pmid: 28529319
- M. Teichert et al., Pericyte-expressed Tie2 controls angiogenesis and vessel maturation. Nat. Commun. 8,16106 (2017). doi: 10.1038/ncomms16106; pmid: 28719590
- T. Stuart et al., Comprehensive integration of single-cell data. Cell 177, 1888–1902.e21 (2019). doi: 10.1016/j.cell.2019.05.031; pmid: 31178118
- M. Ameen et al., Integrative single-cell analysis of cardiogenesis identifies developmental trajectories and non-coding mutations in congenital heart disease. Cell 185, 4937–4953. e23 (2022). doi: 10.1016/j.cell.2022.11.028; pmid: 36563664
- M. Litviňuková et al., Cells of the adult human heart. Nature 588, 466–472 (2020).
 doi: 10.1038/s41586-020-2797-4; pmid: 32971526
- J. D. Hocker et al., Cardiac cell type-specific gene regulatory programs and disease risk association. Sci. Adv. 7, eabf1444 (2021). doi: 10.1126/sciadv.abf1444; pmid: 33990324
- 64. A. L. Koenig et al., Single-cell transcriptomics reveals cell-type-specific diversification in human heart failure. Nat. Cardiovasc. Res. 1, 263–280 (2022). doi: 10.1038/s44161-022-00028-6: pmid: 35959412
- P. Spangenberg et al., Rapid and fully automated blood vasculature analysis in 3D light-sheet image volumes of different organs. Cell Rep. Methods 3, 100436 (2023). doi: 10.1016/j.crmeth.2023.100436; pmid: 37056368
- K. Ronaldson-Bouchard et al., Advanced maturation of human cardiac tissue grown from pluripotent stem cells. Nature 556, 239–243 (2018). doi: 10.1038/s41586-018-0016-3; pmid: 29618819
- X. Yang et al., An intelligent quantification system for fetal heart rhythm assessment: A multicenter prospective study. Heart Rhythm 21, 600–609 (2024). doi: 10.1016/ j.hrthm.2024.01.024; pmid: 38266752
- R. J. Mills et al., Functional screening in human cardiac organoids reveals a metabolic mechanism for cardiomyocyte cell cycle arrest. Proc. Natl. Acad. Sci. U.S.A. 114, E8372–E8381 (2017). doi: 10.1073/pnas.1707316114; pmid: 28916735
- J. K. Ewoldt et al., Induced pluripotent stem cell-derived cardiomyocyte invitro models: Benchmarking progress and ongoing challenges. Nat. Methods 22, 24–40 (2025). doi: 10.1038/s41592-024-02480-7; pmid: 39516564
- D. MacGrogan, J. Münch, J. L. de la Pompa, Notch and interacting signalling pathways in cardiac development, disease, and regeneration. *Nat. Rev. Cardiol.* 15, 685–704 (2018). doi: 10.1038/s41569-018-0100-2; pmid: 30287945
- R. M. Gladden, P. Martinez, P. Seth, Fentanyl law enforcement submissions and increases in synthetic opioid-involved overdose deaths - 27 states, 2013-2014. MMWR Morb. Mortal. Wkly. Rep. 65, 837–843 (2016). doi: 10.15585/mmwr.mm6533a2; pmid: 27560775
- B. T. Bateman et al., Patterns of opioid utilization in pregnancy in a large cohort of commercial insurance beneficiaries in the United States. Anesthesiology 120, 1216–1224 (2014). doi: 10.1097/ALN.0000000000000172; pmid: 24525628
- R. J. Desai, S. Hernandez-Diaz, B. T. Bateman, K. F. Huybrechts, Increase in prescription opioid use during pregnancy among Medicaid-enrolled women. *Obstet. Gynecol.* 123, 997–1002 (2014). doi: 10.1097/AOG.0000000000000208; pmid: 24785852
- T. Delate, M. Hodges, M. Swank, T. Ota, C. L. Pratt, Birth outcomes with prescribed chronic and acute opioid exposure during pregnancy. *J. Opioid. Manag.* 15, 407–415 (2019). doi: 10.5055/jom.2019.0529; pmid: 31849031
- 75. B. Varney et al., Opioid analgesic exposure during the first trimester of pregnancy and the risk of major congenital malformations in infants: A systematic review and meta-analysis[†]. Anaesthesia 79, 967–977 (2024). doi: 10.1111/anae.16307; pmid: 38715235
- A. Deglincerti et al., Self-organization of the invitro attached human embryo. Nature 533, 251–254 (2016). doi: 10.1038/nature17948; pmid: 27144363
- M. N. Shahbazi et al., Self-organization of the human embryo in the absence of maternal tissues. Nat. Cell Biol. 18, 700–708 (2016). doi: 10.1038/ncb3347; pmid: 27144686
- W. Liu et al., Fentanyl stimulates tumor angiogenesis via activating multiple proangiogenic signaling pathways. Biochem. Biophys. Res. Commun. 532, 225–230 (2020). doi: 10.1016/j.bbrc.2020.08.038; pmid: 32861420

Science 5 JUNE 2025 21 of 22

RESEARCH ARTICLE

- N. R. Hannan, C. P. Segeritz, T. Touboul, L. Vallier, Production of hepatocyte-like cells from human pluripotent stem cells. *Nat. Protoc.* 8, 430–437 (2013). doi: 10.1038/ nprot.2012.153; pmid: 23424751
- 80. Y. Guan et al., The phosphatidylethanolamine biosynthesis pathway provides a new target for cancer chemotherapy. J. Hepatol. 72, 746–760 (2020). doi: 10.1016/ j.jhep.2019.11.007; pmid: 31760071
- M. Rezvani et al., Fetal liver-like organoids recapitulate blood-liver niche development and multipotent hematopoiesis from human pluripotent stem cells. bioRxiv, 2024.2010.2011.617794 [Preprint] (2024); https://doi.org/10.1101/2024.10.11.617794.
- E. A. Bulger, I. Muncie-Vasic, A. R. G. Libby, T. C. McDevitt, B. G. Bruneau, TBXT dose sensitivity and the decoupling of nascent mesoderm specification from EMT progression in 2D human gastruloids. *Development* 151, dev202516 (2024). doi: 10.1242/dev.202516; pmid: 38411343
- J. M. Muncie et al., Mechanical tension promotes formation of gastrulation-like nodes and patterns mesoderm specification in human embryonic stem cells. Dev. Cell 55, 679–694. e11 (2020). doi: 10.1016/j.devcel.2020.10.015; pmid: 33207224
- M. Valet, E. D. Siggia, A. H. Brivanlou, Mechanical regulation of early vertebrate embryogenesis. *Nat. Rev. Mol. Cell Biol.* 23, 169–184 (2022). doi: 10.1038/s41580-021-00424-z; pmid: 34754086
- D. Gospodarowicz, H. Bialecki, G. Greenburg, Purification of the fibroblast growth factor activity from bovine brain. J. Biol. Chem. 253, 3736–3743 (1978). doi: 10.1016/ S0021-9258(17)34863-9; pmid: 649600
- 86. T. Su *et al.*, Single-cell analysis of early progenitor cells that build coronary arteries. *Nature* **559**, 356–362 (2018). doi: 10.1038/s41586-018-0288-7; pmid: 29973725
- Y. Miao et al., Intrinsic endocardial defects contribute to hypoplastic left heart syndrome. Cell Stem Cell 27, 574–589.e8 (2020). doi: 10.1016/j.stem.2020.07.015; pmid: 32810435
- K. Kodo et al., iPSC-derived cardiomyocytes reveal abnormal TGF-β signalling in left ventricular non-compaction cardiomyopathy. Nat. Cell Biol. 18, 1031–1042 (2016). doi: 10.1038/ncb3411; pmid: 27642787
- J. Lee et al., Activation of PDGF pathway links LMNA mutation to dilated cardiomyopathy. Nature 572, 335–340 (2019). doi: 10.1038/s41586-019-1406-x; pmid: 31316208
- Y. An, W. Wu, A. Lv, A PCR-after-ligation method for cloning of multiple DNA inserts. *Anal. Biochem.* 402, 203–205 (2010). doi: 10.1016/j.ab.2010.03.040; pmid: 20363207
- D. James et al., Lentiviral transduction and clonal selection of hESCs with endothelialspecific transgenic reporters. Curr. Protoc. Stem Cell Biol. 17, 1F.12.1–1F.12.14 (2011). doi: 10.1002/9780470151808.sc01f12s17; pmid: 21509935
- 92. X. Lian *et al.*, Robust cardiomyocyte differentiation from human pluripotent stem cells via temporal modulation of canonical Wnt signaling. *Proc. Natl. Acad. Sci. U.S.A.* **109**, E1848–E1857 (2012). doi: 10.1073/pnas.1200250109; pmid: 22645348
- Q. Smith et al., Cytoskeletal tension regulates mesodermal spatial organization and subsequent vascular fate. Proc. Natl. Acad. Sci. U.S.A. 115, 8167–8172 (2018). doi: 10.1073/ pnas.1808021115; pmid: 30038020
- H. Aghajanian et al., Coronary vasculature patterning requires a novel endothelial ErbB2 holoreceptor. Nat. Commun. 7, 12038 (2016). doi: 10.1038/ncomms12038; pmid: 27356767
- J. A. Ramilowski et al., A draft network of ligand-receptor-mediated multicellular signalling in human. Nat. Commun. 6, 7866 (2015). doi: 10.1038/ncomms8866; pmid: 26198319
- 96. X. Qin et al., Photoacoustic imaging of embryonic stem cell-derived cardiomyocytes in living hearts with ultrasensitive semiconducting polymer nanoparticles. Adv. Funct. Mater. 28, 1704939 (2018). doi: 10.1002/adfm.201704939; pmid: 30473658
- L. Sala et al., Musclemotion: A versatile open software tool to quantify cardiomyocyte and cardiac muscle contraction invitro and invivo. Circ. Res. 122, e5–e16 (2018). doi: 10.1161/ CIRCRESAHA.117.312067; pmid: 29282212

 O. J. Abilez, Cardiac and hepatic vascularized organoid data and metadata, version 1, Zenodo (2025); https://doi.org/10.5281/zenodo.14959505.

ACKNOWLEDGMENTS

We thank the Stanford Neuroscience Microscopy Service (NMS) (A. Olson, G. Wang), the Stanford Cell Sciences Imaging Facility (CSIF) (J. Mulholland, K. Lee), the Stanford Genomics (SG) Facility (J. Coller, D. Wagh), the Stanford Genetics Bioinformatics Service Center (R. Nair, Y. Zhang), the Computational Services and Bioinformatics Facility (CSBF) (L. Kozar), the Stanford Protein and Nucleic Acid (PAN) Facility, the Stanford Neuroscience Gene Vector and Virus Core (GVVC), the Stanford Department of Physics Student Machine Shop (M. Solyali, K. Merkle) for all their technical support, K. Lam and R. Tully for help with confocal imaging, and R. Bhoi for his help with organoid work. O.J.A. thanks L. Abilez for several fruitful discussions on various aspects of this study. We thank D. James and S. Rafii (Reproductive Endocrinology Laboratory and Ansary Stem Cell Institute, Weill Cornell Medical College) for the pLV-hVPrmOrange plasmid. We thank A. Brivanlou (Laboratory of Synthetic Embryology, Rockefeller University) for the hESC-RUES-GLR line. Funding: This research was supported by NIH grants KO1HL130608 and L30HL138771 (O.J.A.); NIH grants R15HD108720 and R56HL174856 (H.Y.); NIH grant T32GM136501 (A.H.G.); NIH grant K08HL119251 (K.D.W.); NIH grants RO1HL150693, RO1HL141371, RO1HL146690, RO1HL145676, RO1HL176822, RO1HL163680, R01HL171102, U01Al183953, and P01HL141084 (J.C.W.); NIH grants R01HL150414 and R01HL139679 (I.K.); NIH grant K99HL166693 (M.S.) NIH grants R01DC021133 and R240D035408 (G.P.); American Heart Association Postdoctoral Fellowship Award 18POST34030106 (H.Y.); American Heart Association Fellowship Award 23POST1021274 (Z.Y.); Tobacco-Related Disease Research Program (TRDRP) T33FT6330 (Z.Y.); California Institute for Regenerative Medicine grant RC1-00151 (C.K.Z.); a Stanford Maternal & Child Health Research Institute Transdisciplinary Initiatives Program grant (O.J.A.); a Stanford Maternal & Child Health Research Institute Transdisciplinary Initiatives Program grant (D.O.); a Stanford Cardiovascular Institute seed grant (O.J.A. and H.Y.); and Stanford Bio-X Program support (O.J.A.). **Author contributions:** Conceptualization: O.J.A.; Funding acquisition: O.J.A., H.Y., I.K., D.O., G.P., C.K.Z, J.C.W.; Investigation: O.J.A., H.Y., Y.G., M.S., Z.Y., Y.Z., A.H.G., M.E., R.V., S.R.Z., Y.O., M.S., P.N.N., F.J., H.T.W., D.O.; Methodology: O.J.A.; Project administration: O.J.A., H.Y.; Software: O.J.A., L.D., L.T., K.D.W., E.H.L., G.Z., B.A., I.K.; Supervision: O.J.A., H.Y., I.K., D.O., G.P., C.K.Z., J.C.W.; Visualization: O.J.A., H.Y., Y.G., M.S., Z.Y., Y.Z., A.H.G., M.E., L.D., R.V., S.R.Z., L.T., K.D.W., E.H.L., F.J., H.T.W., G.Z., B.A., I.K., D.O.; Writing – original draft: O.J.A., H.Y., J.C.W.; Writing - review & editing: O.J.A., H.Y., M.S., D.O., G.P., C.K.Z., J.C.W. **Competing interests:** Stanford University has filed a patent application "Creation of Vascularized Biological Structures" that covers the generation of vascularized organoids (patent application nos. US 63/314,958, US 18/838,211, CA 3,244,245, and WO 2023/164242) (O.J.A., H.Y., J.C.W.). O.J.A. is a cofounder, president, and equity holder of Bullseye Biotechnologies, a paid consultant of Rosebud Biosciences, and a consultant and equity holder of CytoHub. K.D.W. is a cofounder and chief executive officer of Rosebud Biosciences. E.H.L. is a cofounder and chief technology officer of Rosebud Biosciences. J.C.W. is a cofounder and scientific advisory board member of Greenstone Biosciences. All other authors declare that they have no competing interests. Data and materials availability: Bulk RNA-sequencing and single-cell RNA-sequencing data sets generated for this study are deposited in the Gene Expression Omnibus (GEO) under accession number [GSE185194]. Image data and scripts used for the scRNA-seq analyses are available on Zenodo (98). All other data needed to evaluate the conclusions are available in the main text or the supplementary materials. The hESC-3R line is available from the Stanford CVI Biobank under material transfer agreements with Stanford University and WiCell Research Institute. All hiPSC lines are available from the Stanford CVI Biobank under material transfer agreements with Stanford University. License information: Copyright @ 2025 the authors, some rights reserved; exclusive licensee American Association for the Advancement of Science. No claim to original US government works. https://www.science.org/about/science-licenses-journalarticle-reuse

SUPPLEMENTARY MATERIALS

science.org/doi/10.1126/science.adu9375
Figs. S1 to S16; Tables S1 to S8; Reference (99); Movies S1 to S10; MDAR Reproducibility Checklist

Submitted 30 November 2024; accepted 2 April 2025

10.1126/science.adu9375

Science 5 JUNE 2025 22 of 22